



1 Impact of light-absorbing particles on snow albedo darkening and associated radiative forcing
2 over High Mountain Asia: High resolution WRF-Chem modeling and new satellite observations

3

4 Chandan Sarangi¹, Yun Qian^{1*}, Karl Rittger², Kat J. Bormann³, Ying Liu¹, Hailong Wang¹, Hui
5 Wan¹, Guangxing Lin¹, and Thomas H Painter³

6

7 ¹Pacific Northwest National Laboratory, Richland, WA

8 ²Institute of Arctic and Alpine Research, Boulder, CO

9 ³Jet Propulsion Laboratory, California Institute of Technology, Pasadena, CA

10

11

12

13

14 Submitted to the Atmospheric Chemistry and Physics

15 September 13, 2018

16 Corresponding Author: yun.qian@pnnl.gov

17

18



19 Abstract

20 Light-absorbing particles (LAPs), mainly dust and black carbon, can significantly impact
21 snowmelt and regional water availability over High Mountain Asia (HMA). In this study, for the
22 first time, online aerosol-snow interactions enabled and a fully coupled chemistry Weather
23 Research and Forecasting (WRF-Chem) regional model is used to simulate LAP-induced
24 radiative forcing on snow surfaces in HMA at relatively high spatial resolution (12 km, WRF-
25 HR) than previous studies. Simulated macro- and micro-physical properties of the snowpack and
26 LAP-induced snow darkening are evaluated against new spatially and temporally complete
27 datasets of snow covered area, grain size, and impurities-induced albedo reduction over HMA. A
28 WRF-Chem quasi-global simulation with the same configuration as WRF-HR but a coarser
29 spatial resolution (1 degree, WRF-CR) is also used to illustrate the impact of spatial resolution
30 on simulations of snow properties and aerosol distribution over HMA. Due to a more realistic
31 representation of terrain slopes over HMA, the higher resolution model (WRF-HR) shows
32 significantly better performance in simulating snow area cover, duration of snow cover, snow
33 albedo and snow grain size over HMA, as well as an evidently better atmospheric aerosol
34 loading and mean LAPs concentration in snow. However, the differences in albedo reduction
35 from model and satellite retrievals is large during winter due to associated overestimation in
36 simulated snow fraction. It is noteworthy that Himalayan snow cover have high magnitudes of
37 LAP-induced snow albedo reduction (4-8 %) in summer (both from WRF-HR and satellite
38 estimates), which, induces a snow-mediated radiative forcing of $\sim 30\text{-}50\text{ W/m}^2$. As a result,
39 Himalayas (specifically western Himalayas) hold the most vulnerable glaciers and mountain
40 snowpack to the LAP-induced snow darkening effect within HMA. In summary, coarse spatial
41 resolution and absence of snow-aerosol interactions over Himalaya cryosphere will result in
42 significant underestimation of aerosol effect on snow melting and regional hydroclimate.

43

44

45

46

47



48 1. Introduction

49 Light-absorbing aerosol particles (LAPs; airborne dust and black carbon (BC) specks),
50 can impact on regional water availability over Asia in three ways. Firstly, LAPs can directly
51 interact with incoming solar radiation and induce thermo-dynamical modifications to synoptic
52 scale circulations (Hansen et al., 1997 ; Ramanathan et al., 2001; Bond et al., 2013; Lau et al.,
53 2006; Bollasina et al., 2011; Li et al., 2016). Secondly, acting as cloud condensation nuclei,
54 changes in concentrations of these particles can lead to microphysical modification of cloud
55 systems and precipitations (Fan et al., 2016; Li et al., 2016 ; Qian et al., 2009; Sarangi et al.,
56 2017). Finally, deposition of LAPs in the snowpack can also darken the snow, reduce its surface
57 albedo and accelerate snow warming and melting (Warren and Wiscombe, 1980; Qian et al.,
58 2015; Qian et al., 2011; Qian et al., 2009a; Lau et al., 2010; Xu et al., 2009; Hadley and
59 Kirchstetter, 2012; Dang et al., 2017). Modeling studies have suggested that the LAP-induced
60 snow darkening mechanism has warming and snow-melting efficacy even greater than that of
61 greenhouse gases (GHGs) (Hansen and Nazarenko, 2004; Flanner et al., 2007; Qian et al., 2011;
62 Skiles et al., 2012). To give a perspective, the concentration of just 100 ng of BC in 1 g of
63 snowpack will reduce the visible-wavelength albedo of grain radius 1000 μm by 10% (Fig. 1b of
64 Warren, 2013). A chain of positive feedback mechanisms results in such large impact of LAPs
65 (Qian et al., 2015). Initially, as snow starts to melt, the concentration of LAPs in snowpack
66 increases because a portion of LAPs accumulate at the surface of the snowpack instead of getting
67 washed away with meltwater (Conway et al., 1996; Flanner et al., 2007; Doherty et al., 2010).
68 This increase in LAP concentration leads to enhanced warming of the snowpack and thereby
69 increases the effective snow grain size, which further lowers snow albedo (Warren and
70 Wiscombe, 1980; Hadley and Kirchstetter, 2012). Nonetheless, at higher concentrations, grain



71 sizes can again be reduced due to the loss of mass from surface layers with the intense melting
72 (Painter et al., 2013). As this process continues, sufficient snow melt occurs to expose the darker
73 underlying surface, leading to enhanced warming and snow ablation commonly-known as “snow
74 albedo feedback” (Warren and Wiscombe, 1980; Hansen and Nazarenko, 2004; Flanner et al.,
75 2007; Qian et al., 2015). In turn, this earlier loss of snow cover induces surface warming and
76 perturbing regional circulations (Hansen and Nazarenko, 2004; Lau et al., 2010; Qian et al.,
77 2011). This LAP-induced modification of snow albedo feedback is identified as one of major
78 forcing agents affecting climate change with a high level of uncertainty (IPCC, 2013).

79 High Mountain Asia (HMA) includes the Tibetan plateau, central Asian mountains and
80 the Himalaya cryosphere. It holds the largest glacial cover (~9500 glaciers) outside the polar
81 region (Dyurgerov, 2001). Observations revealed that a historical decadal increase in the surface
82 air temperature over HMA in a range of 0.6-1.8 °C (Shrestha et al., 1999; Wang et al., 2008), and
83 the warming is faster over higher elevations (> 4000 m) in the last three decades (Xu et al.,
84 2009b; Ghatak et al., 2014). The Himalaya glacier area has cumulatively decreased by ~16%
85 during the period 1962 to 2004 (Kulkarni et al., 2010) and the spring snow cover is decreasing at
86 a decadal rate of ~0.8 million km² during the last 50 years (Brown and Robinson, 2011). The
87 average retreat rate on the north slope of Mount Everest is as high as 5.5–9.5 m y⁻¹ (Ren et al.,
88 2006). The Himalaya cryosphere contributes to the stream flow in Indus and Ganges river
89 systems by ~ 50 % and ~10-30%, respectively (Khan et al., 2017). Warming and glacier retreat
90 over the Himalaya cryosphere have a great potential to impact the fresh water availability for
91 about 700 million people, modify regional hydrology, and disturb the agrarian economy of all
92 South Asian countries (Bolch et al., 2012; Immerzeel et al., 2010; Kaser et al., 2010; Singh and



93 Bengtsson, 2004; Barnett et al., 2005; Yao et al., 2007). Therefore, it is critical to disentangle the
94 factors contributing to glacier retreat and snow melt over HMA.

95 Regional warming due to increasing greenhouse gases (Ren and Karoly, 2006) has been reported
96 as the primary cause of the high rate of warming and glacier retreat over HMA. However, in the
97 last decade, advancement in remote sensing and availability of measurements from several field
98 campaigns suggest that the contribution of LAP loading (in the atmosphere) to the warming and
99 glacier melting over HMA is probably greater than previously believed (Ramanathan et al.,
100 2007; Prasad et al., 2009; Menon et al., 2010). Continuous observations over the Nepal Climate
101 Observatory Pyramid (NCO-P) facility located at 5079 m a.s.l. in the southern foothills of Mt.
102 Everest revealed very high concentrations of black carbon (Marcq et al., 2010) and desert dust
103 (Bonasoni et al., 2010) especially in spring from Indo-Gangetic plains. Atmospheric LAPs are
104 scavenged to the snow/ice surface by dry and wet deposition and cause measurable snow
105 darkening and melting (Gautam et al., 2013; Yasunari et al., 2010b; Yasunari et al., 2013; Nair et
106 al., 2013; Ménégos et al., 2014; Ming et al., 2008; Flanner and Zender, 2005). Thus, LAP
107 deposited in snow and associated snow darkening has been suggested as a key factor to the early
108 snowmelt and rapid glacier retreat over HMA (Yasunari et al., 2010; Ming et al., 2008; Xu et al.,
109 2009a; Flanner et al., 2007; Qian et al., 2011).

110 While previous studies have underlined the significance of LAP-deposition in snow over
111 HMA, the estimation of LAP-induced snow darkening and associated radiative forcing is still
112 highly uncertain (Qian et al., 2015). Many of these studies used online global model simulations
113 at coarse spatial resolutions of ~50-150 km (Flanner and Zender, 2005; Ming et al., 2008; Qian
114 et al., 2011). Others used offline simulation of the snow albedo effect using measured
115 concentrations of deposited LAP in surface snow or estimated from atmospheric loading and ice



116 cores (Yasunari et al., 2013; Nair et al., 2013; Wang et al., 2015). The complex terrain of HMA,
117 seasonal snowfall and near surface air circulation are not well resolved by coarse global climate
118 models (Kopacz et al., 2011; Ménégoz et al., 2014). Similarly, offline estimations are limited in
119 scope because they are site specific and are based on simplified assumptions about deposition
120 rates. Ideally, online high resolution simulations allowing for LAP-snow interactions should
121 facilitate a more realistic understanding of LAP deposition to snow and LAP-induced snow
122 darkening effect in terms of both magnitude and spatial variability over HMA.

123 In this study, a modified version of the online chemistry coupled with Weather Research
124 and Forecasting regional model (WRF-Chem v3.5.1), which, is then fully coupled with SNICAR
125 (SNOW, ICe, and Aerosol Radiative) model, is used to perform first-ever high resolution (12 km)
126 simulation over the HMA region for the water year 2013-14 (October 1, 2013 to September 30,
127 2014). Satellite observations of snow properties like snow albedo, grain size, and LAP-induced
128 snow darkening from MODSCAG and MODDRFS retrievals are used for evaluation (Painter et
129 al., 2009; 2012). The main objective of this study is to evaluate the skill of high resolution WRF-
130 Chem model in simulating properties of snowpack, aerosol distribution, LAP in snow and LAP-
131 induced snow darkening over HMA using spatially and temporally complete (STC) remotely
132 sensed snow surface properties (SSP) from MODIS (Dozier et al, 2008; Rittger et al, 2016). Our
133 second objective is to demonstrate the benefit for aerosol and snow distributions in high
134 resolution runs by comparing to a coarse gridded quasi-global model simulation over HMA. This
135 quasi-global simulation is run with the same WRF-Chem configuration but at 1 degree spatial
136 resolution. Finally, the spatiotemporal variation of simulated LAP deposition, snow albedo
137 darkening and snow mediated LAP radiative forcing (LAPRF) over HMA are discussed. The



138 model details and datasets used are described in Section 2. Results and discussions are presented
139 in Section 3 followed by conclusions in Section 4.

140 **2: Model simulations and observational datasets**

141 Below, we provide details on the aerosol module used in WRF-Chem, interactive
142 coupling with aerosol and SNICAR via land model, and the model setup for both 12 km and 1
143 degree resolution runs. The details for the remote sensing observations that are used to evaluate
144 the models are also provided.

145 **2.1: Coupled WRF-Chem-CLM-SNICAR Model description**

146 The WRF-Chem simulation is performed at 12 km × 12 km horizontal resolution
147 (hereafter refereed as WRF-HR) with 210 × 150 grid cells (64–89°E, 23–40°N) (Figure 1) and
148 35 vertical layers. The simulation was conducted from 20th September, 2013 to 30th September,
149 2014, to provide one year of results (following a 10-day model spin-up). ERA-interim reanalysis
150 data at 0.7° horizontal resolution and 6 h temporal intervals are used for meteorological initial
151 and lateral boundary conditions. The simulation is re-initialized every 4th day to prevent the drift
152 of model meteorology. Model physics options used are the MYJ (Mellor–Yamada– Janjic)
153 planetary boundary layer scheme, Morrison 2-moment microphysics scheme, community land
154 model (CLM), Kain-Fritsch cumulus scheme and Rapid Radiative Transfer Model for GCMs
155 (RRTMG) for longwave and shortwave radiation schemes.

156 The CBM-Z (carbon bond mechanism) photochemical mechanism (Zaveri and Peters,
157 1999) coupled with eight bin MOSAIC (Model for Simulating Aerosol Interactions and
158 Chemistry) aerosol model (Zaveri et al., 2008) is used. This is the most sophisticated aerosol
159 module available for the WRF-Chem model. The sectional approach with eight discrete size bins



160 is used to represent the size distributions of all the major aerosol components (including sulfate,
161 nitrate, ammonium, black carbon (BC), organic carbon (OC), sea salt, and mineral dust) in the
162 model. The processes of nucleation, condensation, coagulation, aqueous phase chemistry, and
163 water uptake by aerosols in each bin size are included in the MOSAIC module. Dry deposition of
164 aerosol mass and number is simulated by including both diffusion and gravitational effects as per
165 Binkowski and Shankar (1995). Wet removal of aerosols follow Easter et al. (2004) and
166 Chapman et al. (2009) and includes grid resolved impaction and interception processes for both
167 in-cloud (rainout) and below-cloud (washout) aerosol removal. Processes involved in convective
168 transport and wet removal of aerosols by cumulus clouds are described in Zhao et al. (2013).

169 Anthropogenic emissions used in our study is at $0.5^{\circ} \times 0.5^{\circ}$ horizontal resolution and are
170 taken from the NASA INTEX-B mission Asian emission inventory for year 2006 (Zhang et al.,
171 2009). Biomass burning emissions at $0.5^{\circ} \times 0.5^{\circ}$ horizontal resolution for the water year 2013-14
172 are obtained from the Global Fire Emissions Database, Version 3 (GFEDv3) (Van Der Werf et
173 al., 2010), which are vertically distributed in our simulation using the injection heights
174 prescribed by Dentener et al. (2006) for the Aerosol Inter Comparison project (AeroCom). Sea
175 salt and dust emissions follow Zhao et al. (2014). Dust surface emission fluxes are calculated
176 with the Georgia Institute of Technology-Goddard Global Ozone Chemistry Aerosol Radiation
177 and Transport (GOCART) dust emission scheme (Ginoux et al., 2001), and emitted into the eight
178 MOSAIC size bins with respective mass fractions of 10^{-6} , 10^{-4} , 0.02, 0.2, 1.5, 6, 26, and 45%.

179 Aerosol optical properties are computed as a function of wavelength for each model grid
180 cell. The Optical Properties of Aerosols and Clouds (OPAC) data set (Hess et al., 1998) is used
181 for the shortwave (SW) and longwave (LW) refractive indices of aerosols and a complex
182 refractive index of aerosols (assuming internal mixture) is calculated by volume averaging for



183 each chemical constituent of aerosols for each bin. A spectrally-invariant value of $1.53 \pm 0.003i$
184 is used for the SW complex refractive index of dust. Fast et al. (2006) and Barnard et al. (2010)
185 provide detailed descriptions of the computation of aerosol optical properties such as extinction
186 coefficient, single scattering albedo (SSA), and asymmetry factor in WRF-Chem. Following
187 Zhao et al. (2011) and Zhao et al. (2013a), aerosol radiative feedback is coupled with the Rapid
188 Radiative Transfer Model (RRTMG) (Mlawer et al., 1997) and the direct radiative forcing of
189 individual aerosol species in the atmosphere are diagnosed. Aerosol–cloud interactions are
190 included in the model following Gustafson et al. (2007).

191 The increasingly used Snow, Ice, and Aerosol Radiation (SNICAR) model simulates the
192 snow properties and associated radiative heating rates of multilayer snow packs (Flanner and
193 Zender, 2005; Flanner et al., 2009, 2012 and 2007). Fundamentally, it employs the snow albedo
194 theory (parameterization) based on Warren and Wiscombe (1980) and the two-stream radiative
195 approximation for multilayers from Toon et al. (1989). SNICAR can also simulate aerosol
196 radiative effect in snow for studying the LAP heating and snow aging (Flanner et al., 2007).
197 Recently, laboratory and site measurements are used to validate the SNICAR simulated change
198 of snow albedo for a given BC concentration in snow (Hadley and Kirchstetter, 2012; Brandt et
199 al., 2011). For radiative transfer calculations, SNICAR defines layers matching with the five
200 thermal layers in community land model (CLM) that vertically resolve the snow densification
201 and meltwater transport (Oleson et al., 2010). In WRF-Chem-SNICAR coupled model, BC and
202 dust deposition on snow is calculated in a prognostic approach through dry and wet deposition
203 processes. BC in snow can be represented as externally and internally mixed with precipitation
204 hydrometeors depending on the removal mechanism involved, but dust is considered to only mix
205 externally with snow grains (following Flanner et al., 2012). SNICAR in WRF-Chem simulates



206 four tracers of dust based on size (with diameters of 0.1–1, 1–2.5, 2.5–5, and 5–10 μm) and two
207 tracers of BC (externally and internally mixed BC with 0.2 μm dry diameter) in snow. The
208 MOSAIC aerosol model simulates dust in the atmosphere with eight size bins (0.039–0.078,
209 0.078–0.156, 0.156–0.312, 0.312–0.625, 0.625 - 1.25, 1.25–2.5, 2.5–5.0, and 5.0–10.0 μm in dry
210 diameter). The first 4 bins are coupled with the smallest bin of dust particles in SNICAR. While
211 the next two MOSAIC bins (5th and 6th) map into the second bin of SNICAR, the 7th and 8th
212 MOSAIC dust bins correspond to the third and fourth SNICAR dust bins (Zhao et al., 2014),
213 respectively. Deposition of LAPs to snow in SNICAR are immediately mixed in the CLM
214 surface snow layer (< 3 cm). CLM adds excess water in the layer above to the layer beneath
215 during melting. The scavenging of aerosols in snow by meltwater is assumed to be proportional
216 to its mass mixing ratio of the meltwater multiplied by a scavenging factor. Scavenging factors
217 for externally mixed BC and internally mixed BC are assumed to be 0.03 and 0.2, respectively,
218 and 0.02, 0.02, 0.01, and 0.01 for the four dust bins (all externally mixed). Although these
219 scavenging factors are comparable to observations (Doherty et al., 2013), the scavenging ratios
220 can be highly heterogeneous and introduce high uncertainty into the estimation of LAP
221 concentrations in snow (Flanner et al., 2012; Qian et al., 2014). More detailed description about
222 the aerosol deposition and mixing processes, computation of optical properties of snow and
223 LAPs in WRF-Chem-CLM-SNICAR coupling can be found in Zhao et al.(2014) and Flanner et
224 al.(2012).

225 Configured in the way similar to the WRF-HR, a coarse ($1^\circ \times 1^\circ$) gridded WRF-Chem
226 simulation is also performed using a quasi-global model (hereafter referred as WRF-CR) with
227 360×130 grid cells ($180^\circ \text{W} - 180^\circ \text{E}$, $60^\circ \text{S} - 70^\circ \text{N}$). Periodic boundary conditions are used in
228 the zonal direction. Reanalysis of the TROpospheric (RETRO) anthropogenic emissions for the



229 year 2010 (<ftp://ftp.retro.enes.org/pub/emissions/aggregated/anthro/0.5x0.5/>) is used for
230 anthropogenic aerosol and precursor gas emissions in the coarse gridded quasi-global WRF-
231 Chem simulation except for Asia and the United States. INTEX-B anthropogenic emissions
232 (Zhang et al., 2009) and US National Emission Inventory are used for Asia and the U.S.,
233 respectively. Emissions of biomass burning aerosols, sea salt, and dust are treated in the same
234 way as described above for the WRF-HR simulation. More details about the quasi-global WRF-
235 Chem simulation can be found in (Zhao et al., 2013b);Hu et al., 2016). Chemical initial and
236 boundary conditions to the WRF-HR simulation are provided by this quasi-global WRF-CR runs
237 for the same time period to include long-range transported chemical species.

238 **2.2: Aerosol Optical Depth (AOD) dataset**

239 The aerosol robotic network (AERONET – <https://aeronet.gsfc.nasa.gov>) is a global
240 network of ground based remote sensing stations that provides quality-controlled measurements
241 of AOD with uncertainties ~ 0.01 under clearsky conditions over India (Holben et al., 1998;
242 Dubovik et al., 2000). CIMEL Sun scanning spectral radiometers are used to measure direct Sun
243 radiance at eight spectral channels (340, 380, 440, 500, 675, 870, 940, and 1020 nm) and
244 measure spectral columnar AOD (Holben et al., 1998). AERONET provides measurements at
245 ~ 15 min temporal resolution from sunrise to sunset.

246 Skyradiometer Network (Skynet) is another global network of ground based spectral
247 scanning radiometer (POM-01L, Prede, Japan) stations that provides quality-controlled
248 measurements of AOD (Nakajima et al., 1996). With an automatic sun scanner and sensor, it
249 measures sky irradiance in five wavelengths i.e. 400, 500, 675, 870, and 1020 nm. The measured
250 monochromatic irradiance data is processed by using Skyrad.Pack version 4.2 software.
251 Calibration of the Sky radiometer is carried out on a monthly basis (<http://atmos3.cr.chiba->



252 u.jp/skyonet/data.html). Details of the instrumentation and software protocol can be found in
253 Campanelli et al. (2007) and Ningombam et al., (2015). In this study, we have also used AOD
254 measurements at 500 nm over MERAK, a high altitude Skynet station in Himalaya for water
255 year 2013-14.

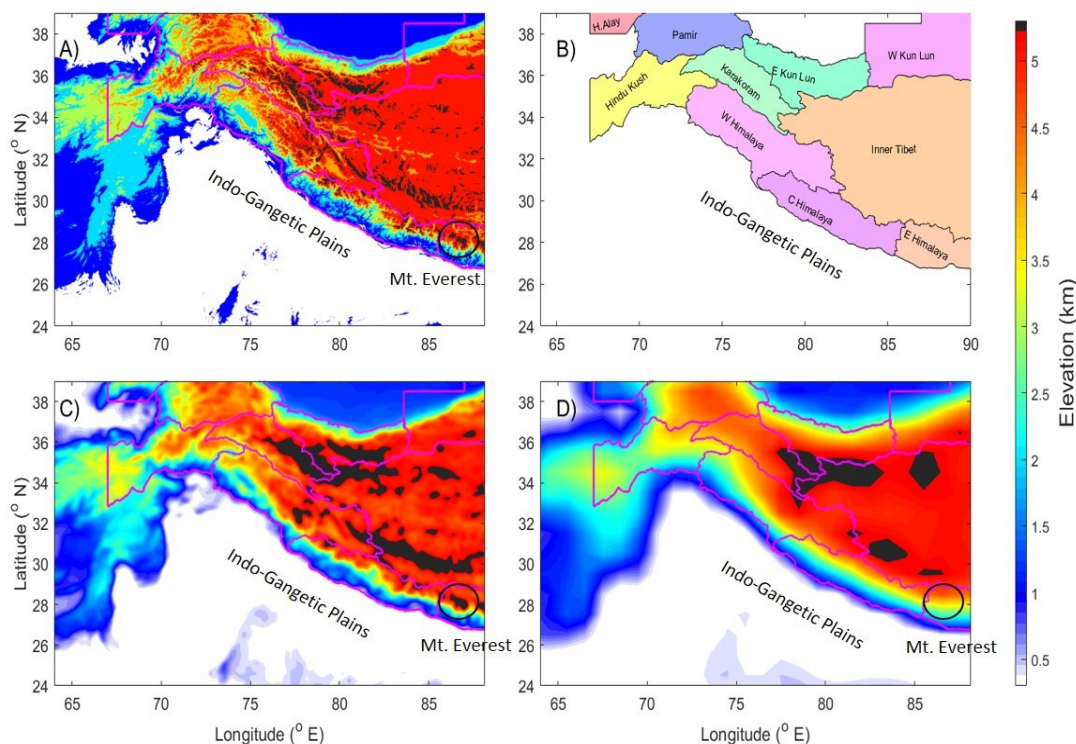
256 The MODerate resolution Imaging SpectroRadiometer (MODIS) instrument onboard the
257 NASA AQUA satellite provides global coverage of daily radiance observations (at 1330 LT) in
258 36 spectral channels. Over North India, Tripathi et al., (2005) has shown that MODIS
259 observations correlate well with ground based measurements. For the evaluation of model
260 simulated AOD, 1° gridded Level 3 AOD estimates (collection 6) at 0.55 μm wavelength
261 obtained from the MODIS instrument are used during water year 2013-14. However, the MODIS
262 land aerosol algorithm uses a dark target approach (Levy et al., 2007), which, is known to have
263 large uncertainties over arid and mountainous surfaces (Levy et al., 2010).

264 **2.3: Spatially and temporally complete MODSCAG and MODDRFS retrievals**

265 Subpixel snow-covered area and snow grain size are retrieved from MODIS-observed
266 surface reflectance data using the physically based MODIS Snow-Covered Area and Grain size
267 (MODSCAG) (Painter et al., 2009) algorithm. In each snow covered pixel, MODSCAG
268 attributes a fractional snow-covered area and grain size using spectral mixture analysis to
269 determine proportion of the pixel that is snow and is not snow. MODSCAG is more accurately
270 identifies snow cover throughout the year than the widely used MODIS snow product:
271 MOD10A1 (Rittger et al., 2013). The MODSCAG snow-mapping algorithm for fraction of snow
272 covered area has an uncertainty of $\sim 5\%$ (Rittger et al., 2013). The current study incorporates
273 pixel level snow cover area and snow grain size from MODSCAG over the HMA region to
274 evaluate snow pack simulation and LAP-induced albedo reduction. Further, MODIS Dust



275 Radiative Forcing in Snow (MODDRFS) model (Painter et al., 2012) is used to determine the
276 LAP-induced albedo reduction over HMA. MODDRFS uses spectral reflectance differences
277 between the measured snow spectral albedo and the modeled clean snow spectral albedo. The
278 pixel level clean snow spectrum corresponding to MODSCAG retrieved snow grain sizes is
279 calculated using discrete ordinate radiative transfer solutions for visible wavelengths and solar
280 zenith angles. Coupled, these products provide the determination of snow albedo for the
281 fractional snow cover with LAP inclusion. Reflectance inputs to MODSCAG and MODDRFS
282 are degraded by cloud cover, off-nadir views, and data errors, but can be filtered in time and
283 space to improve data quality and consistency. Our method for spatially cleaning and filling
284 (Dozier et al., 2008; Rittger et al., 2016) combines noise filtering, snow/cloud interpolation and
285 smoothing to improve the daily estimates snow surface properties (SSP). Using remotely sensed
286 forest height maps (Simard et al., 2011) and MODSCAG vegetation fraction, we adjust the
287 satellite viewable snow cover to account for snow under tree canopy (Rittger et al., 2016). We
288 weight the observations based on satellite viewing angle that varies from 0 to 65 degree with
289 larger uncertainties in off-nadir views (Dozier et al., 2008). The result is a set of spatially and
290 temporally complete (STC) SSPs. Use of these products in an energy balance model to estimate
291 snow water equivalent based on reconstruction produced more accurate snow cover than the
292 Snow Data Assimilation System (SNODAS) or an interpolation of observations from snow
293 pillows (Bair et al., 2016). In this study we use STC versions of MODSCAG and MODDRFS
294 when comparing our WRF model output. The incomplete remotely sensed would be difficult to
295 use given the gaps in data and uncertainties related to viewing angle (Dozier et al., 2008).
296 Hereafter, the use of MODSCAG and MODDRFS terms will invariably refer to these STC-
297 MODSCAG and STC-MODDRFS products.



298

299 Figure 1: Panel A illustrates the terrain elevation at 1 km resolution from ETOPO1 dataset. Panel
300 B shows glacier classification over HMA region used in this study following Randolph Glacier
301 Inventory. Panels C and D illustrate terrain representation in WRF-HR run (12 km) and WRF-
302 CR (1 degree) runs, respectively. For reference, Mt. Everest (shown as black circle in Figure 1C)
303 is distinctly represented in Panel A and C, but not in Panel B.

304

305 **2.4: Variation in terrain representation in WRF-HR and WRF-CR**

306 Figure 1A illustrates the variations in terrain height over HMA at a resolution of 1 arc
307 using ETOPO1 Global Relief Model, a publicly available global topographical dataset (Amante
308 and Eakins, 2009). It clearly shows the enormous relief in terrain as we move from the Indo
309 Gangetic plains (IGP) to the crest of the Himalaya and into the Tibetan Plateau (TP). The
310 majority of HMA is above 4 km altitude with many Himalaya peaks at an altitude higher than 6
311 km. Figure 1B illustrates the mountain ranges and glaciers classified as per the Randolph Glacier



312 Inventory in the Fifth Assessment Report of the Intergovernmental Panel on Climate Change
313 (Pfeffer et al., 2014). Specifically, Pamirs, Hindu Kush, Karakoram, Kunlun, and Himalaya hold
314 the most number of glaciers in HMA. Figures 1C and 1D illustrate the representation of terrain
315 elevation in WRF-HR and WRF-CR, respectively. Compared to Figure 1A, location of mountain
316 peaks (altitude > 5.5 km) are better represented in WRF-HR compared to WRF-CR, as is
317 particularly evident over the Karakoram, Kunlun, and Himalaya ranges. Moreover, the steep rise
318 in elevation between IGP and TP is also well represented by WRF-HR, whereas it is more
319 gradual in WRF-CR.

320 **2.5: Methodology**

321 Simulation of the snow macro- and micro-physical properties, aerosol loading and LAP
322 in snow concentration from WRF-HR, WRF-CR and observational estimates (datasets described
323 above) over HMA are compared in Section 3.1 and Section 3.2. In Section 3.3, the WRF-HR
324 simulated LAP-induced snow albedo reduction values over HMA is compared with
325 corresponding MODIS satellite based STC-MODSCAG and STC-MODDRFS. Lastly, a
326 discussion on the high resolution model simulated LAP-induced radiative forcing estimates over
327 HMA is also presented in context to previous studies and other atmospheric forcing.

328 The simulated fractional snow covered area (fSCA), duration of snow cover over a grid
329 in terms of number of snow cover days (NSD), snow albedo (α) and snow grain sizes (SGS) and
330 LAP-induced snow albedo darkening ($\Delta\alpha$) for midday (1000 -1400 LT) conditions from both the
331 WRF models are compared with corresponding STC-MODSCAG and STC-MODDRFS
332 retrievals over HMA. The number of snow cover days (NSD: defined as days having fSCA
333 values ≥ 0.01) during water year 2013-14 is determined over each grid from STC-MODSCAG
334 and both model runs. They are compared with corresponding values from STC-MODSCAG



335 retrievals, which, are observed during Terra overpasses at 10:30 LT. We have used a window
336 from 10:00 LT to 16:00 LT for representing midday averages of modelled variables to
337 incorporate the variability due to differences in timing (between model and real scenario) of
338 weather conditions like precipitation and clouds. In addition, the change in snow albedo during
339 10:00 - 14:00 LT is < 0.01 (Bair et al., 2017), which, is low compared to other model physics-
340 and data retrieval related uncertainties. The WRF-CR simulated variables and STC-MODSCAG
341 and STC-MODDRFS retrievals are gridded to the resolution of WRF-HR (12 km) for ease of
342 comparison. We have compared annual mean values as well as seasonal mean values for winter
343 (December - February) and summer (April - June) season, separately. We have not considered
344 the monsoon period in our analyses because the snow cover during the monsoon is negligible
345 (except in glaciated regions at high altitudes) relative to other months (Figure S1). To evaluate
346 spatial heterogeneity in our model, the seasonal and annual distribution of these variables are
347 calculated separately for each sub region (shown in Figure 1) within HMA. In addition, to gain
348 an understanding of the extent of temporal variability present in LAP-induced effects, we have
349 also presented daily midday variation in LAP-induced snow darkening and LAP-induced
350 radiative forcing at surface over Chotta Shingri glacier region (32.1-32.35 °N, 77.4-77.7 °E)
351 located in the Chandra–Bhaga river basin of Lahaul valley, Pir Panjal range, in Western
352 Himalayas. It is an accessible and representative site for glacier mass balance studies in western
353 Himalayas. Chotta Shigri glacier has a cumulative glaciological mass loss of -6.72 m w.e.
354 between 2002 and 2014 (Azam et al., 2016).

355 The simulated aerosol optical depth (AOD) is compared with available in-situ
356 observations (described in Section 2.2). Here, quality assured (Level 2) midday (1000 to 1400
357 LT) averages of AOD (550 nm) at seven AERONET stations (Lahore, Jaipur, Kanpur, Gandhi



358 college, Kathmandu and CAS) and one SkyNet site within our study region are used to evaluate
359 the simulated AOD values. Further, the simulated distribution of LAP concentration in snow at a
360 few sites is compared with field measurements. Only a few field measurements of concentration
361 of BC (LAP_{BC}) and dust particles (LAP_{dust}) in the snow surface or the surface layer are available
362 over glaciated regions within our study domain. In this study, measurements of LAP_{BC} over
363 Muztagh Ata in eastern slopes of Pamirs (Xu et al., 2006), Uttaranchal region of W. Himalayas
364 (Svensson et al., 2018), East Rongbuk at 6.4 km altitude (Ming et al., 2012; Ming et al., 2008;
365 Xu et al., 2009a) and composite of recent in-situ measurements from various studies near the
366 NCO-pyramid site in Nepal at 5-6 km altitude (Kaspari et al., 2014; Yasunari et al., 2013; Jacobi
367 et al., 2015; Ginot et al., 2014) is used. Similarly, the point measurements used for evaluating
368 LAP_{dust} are over Abramov glacier in western slopes of Pamirs (Schmale et al., 2017), Muztagh
369 Ata in eastern slopes of Pamirs (Wake et al., 1994), East Rongbuk (Ming et al., 2012) and near
370 NCO-pyramid station (Ginot et al., 2014), respectively.

371 **3: Results and Discussions**

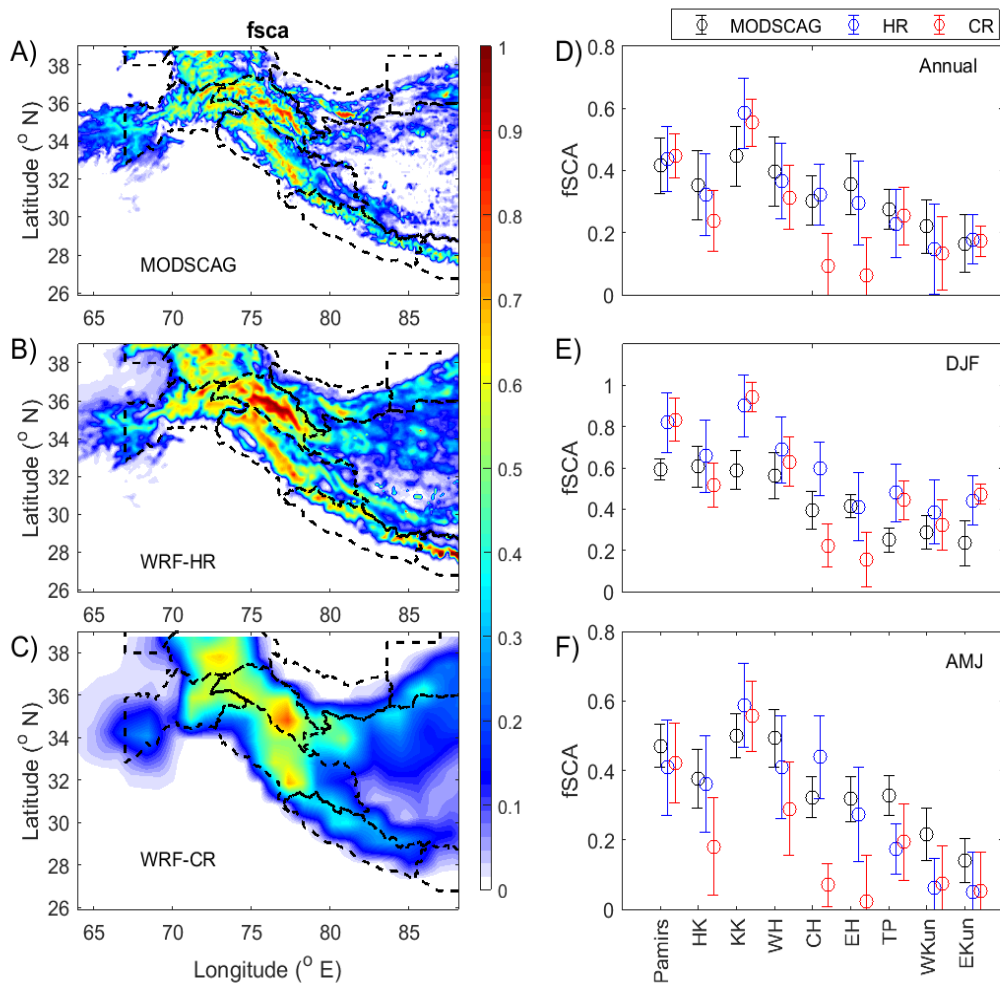
372 **3.1: Snow physical, microphysical and optical properties**

373 The largest values of region-averaged annual mean fSCA within HMA are observed in both the
374 satellite retrievals and the model runs over the Karakoram region (mean=0.45) followed by
375 Pamirs, Himalayas and Hindu Kush in the HMA region (Figures 2A and 2B). In comparison, the
376 fSCA over Kunlun and TP are lower (<0.3), but, pockets of very high fSCA (~0.7) are visible
377 over the west Kunlun ranges (Figure 2A). The annual mean fSCA values and the fine spatial
378 variability are well simulated by WRF-HR (Figure 2B) over the entire HMA region. Of
379 exception are simulations over the Karakoram, where WRF-HR overestimates annual mean
380 fSCA, however, the distribution of annual mean fSCA from WRF-HR and STC-MODSCAG



381 agree in all the sub regions (Figure 2D). This observation is largely valid also for summer
382 months (Figure 2F). But, significant overestimation in distribution of fSCA (by >0.2) during
383 winter is present over Pamirs, Karakoram, W. Himalayas, TP and Kunlun region (Figures 2E).
384 STC-MODSCAG retrievals illustrate that the Pamirs (NSD=230 days) and Karakoram
385 (NSD=270 days) ranges remain snow covered for 7-9 months of the year (Figure 3A). Similarly,
386 the grids in Hindu Kush (NSD=194), W. Himalayas (NSD=189 days) and C. Himalayas
387 (NSD=191 days) are snow covered for ~ 6-7 months. Mountains in E. Himalayas (NSD=142
388 days) remain snow covered for only 4-5 months of the year. The distribution of annual NSD
389 values simulated by WRF-HR in each sub region is close to STC-MODSCAG values (Figure
390 3D). Also, the spatial distribution and magnitude of simulated NSD by WRF-HR is similar to
391 that from STC-MODSCAG for different seasons, separately (Figure S2). Thus, overestimation of
392 annual mean fSCA in WRF-HR during winter is not due to mere averaging error associated with
393 underestimation in simulated NSD during winter (Figure S2).

394



395

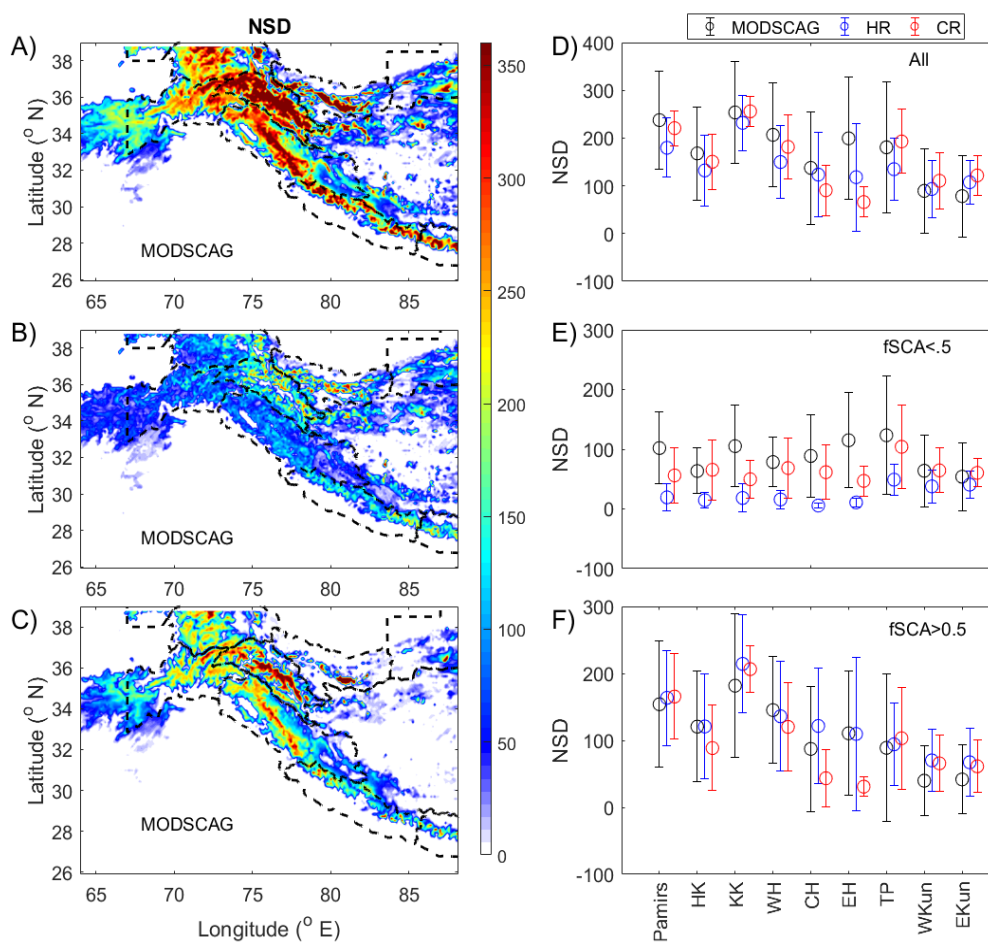
396 Figure 2: Spatial distribution of annual mean snow cover fraction (fSCA) during midday (1000-
 397 1400 LT) for water year 2013-14 from A) STC-MODSCAG retrievals, B) simulated values from
 398 WRF-HR and C) WRF-CR simulations. Panels D-F illustrate the distribution of midday mean
 399 fSCA over each subregion identified by glacier classification following Randolph Glacier
 400 Inventory (X-axis). The circle and vertical legs represent mean ± standard deviation over each
 401 region for D) entire year, E) winter (December - February) and F) summer (April - June)
 402 season, separately. Here, Hindu Kush, Karakoram, W.Himalayas, C.Himalayas, E.Himalayas, Tibetan
 403 Plateau, West Kunlun and East Kunlun regions are abbreviated as HK, KK, WH, CH, EH, TP,
 404 WKun and EKun, respectively.

405



406 We also calculated the number of days of snow cover with low fSCA (<0.5; Figure 3B)
407 and high fSCA (>0.5; Figure 3C) values, separately. The grids in Kunlun, Northern slope of
408 Karakoram, eastern slope of Pamirs and TP region are dominated by snow cover of relatively
409 low fSCA for most of their snow cover duration (Figure 3B). But, grids in Hindu Kush,
410 Himalayas and southern slopes of Karakoram are generally covered with high fSCA values
411 throughout the year (Figure 3C). The distribution of simulated NSD values over each sub region
412 for low and high fSCA scenario is shown in Figures 3E and 3F, respectively. WRF-HR can well
413 simulate the NSD over grids with high fSCA (Figure 3F) but significantly underestimates NSD
414 over grids with low snow cover (Figure 3E). Note that the regions dominated by low annual
415 fSCA in this water year are actually the same regions where WRF-HR simulated fSCA values
416 are being overestimated in winter (Figure 2E). Thus, simulation of fewer number of days with
417 low fSCA (and vice versa) in WRF-HR might also be contributing partially to the overestimation
418 of winter fSCA simulated in WRF-HR compared to STC-MODSCAG. Interestingly, WRF-CR
419 simulated NSD values for low fSCA case is in better agreement with STC-MODSCAG values
420 (Figure 3E). Winter mean distribution of WRF-CR simulated fSCA over Kunlun, W.Himalaya
421 and TP region better match STC-MODSCAG values than the corresponding WRF-HR simulated
422 fSCA values (Figure 2F). It is noteworthy that these subregions (which are dominated by low
423 fSCA grids) receive snowfall from western disturbances during winter months. The cloud cover
424 associated with the western disturbances over these sub regions are extensive in winter which
425 also introduces uncertainty in MODSCAG retrievals and STC processing and contributes to the
426 differences between WRF-HR and MODSCAG in fSCA.

427



428

429 Figure 3: Spatial distribution of snow duration in terms of NSD from A) STC-MODSCAG
 430 retrievals. Panel B and C are similar to Panel A, but, shows number of days when fSCA is below
 431 and above 0.5 over each grid, respectively. Panels D illustrate the distribution of NSD over each
 432 sub region identified by glacier classification following Randolph Glacier Inventory. The circle
 433 and vertical legs represent mean \pm standard deviation over each region for entire year. Here,
 434 Hindu Kush, Karakoram, W.Himalayas, C.Himalayas, E.Himalayas, Tibetan Plateau, West
 435 Kunlun and East Kunlun regions are abbreviated as HK, KK, WH, CH, EH, TP, WKun and
 436 EKun, respectively. Panel E and F are similar to Panel D, but, for NSD corresponding to fSCA
 437 values below and above 0.5, respectively.

438

439 Comparison between performance of WRF-CR and WRF-HR for fSCA clearly show
 440 significant improvements in the WRF-HR simulations over the Hindu Kush and Himalayan



441 ranges (Figure 2D). For instance, the simulated annual mean fSCA in WRF-CR around Mt.
442 Everest (shown as black circle in Figure 1) is less than 0.1 (Figure 2C). This is contrary to the
443 high fSCA values observed at Mt. Everest (0.7 in Figures 2A) and simulated by WRF-HR (0.7 in
444 Figures 2B). Moreover, the improvement is present in both winter and summer months
445 indicating it's independence from meteorological variations (Figures 2E and 2F). Analysis of
446 NSD values indicate that the snow cover duration in WRF-HR also improved significantly over
447 these slopes (Figure S3) irrespective of the season. Note that WRF-CR underestimates the snow
448 duration over Hindu Kush and Himalayas by ~2-6 months (Figure S3) and the spatial location of
449 grids with very high annual mean fSCA values (mountain ranges) improved in WRF-HR
450 compared to the STC-MODSCAG data (Figures 2A-C). The observed improvement in fSCA and
451 NSD simulation over the slopes of Himalaya and Hindu Kush can be attributed to better terrain
452 representation in WRF-HR.

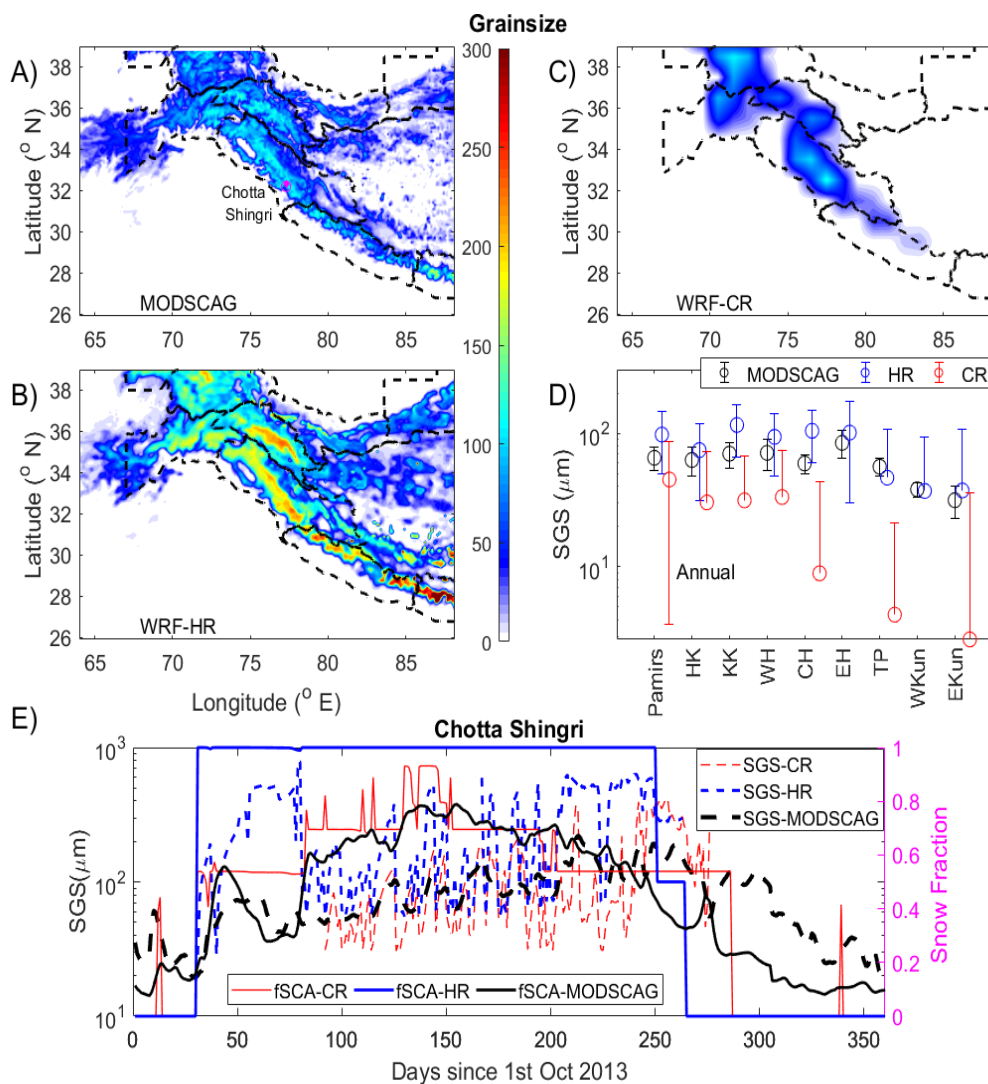
453 Next, the simulated microphysical properties of the snow pack are evaluated against the
454 remote sensing retrievals. Spatial patterns in annual mean SGS from STC-MODSCAG are
455 similar to that seen in fSCA with highest values over the Karakoram and Himalayan ranges
456 (Figures 4A) corresponding to the highest elevations and likely the coldest temperatures
457 hindering snow grain growth. This spatial distribution of annual mean SGS values is well
458 simulated in WRF-HR runs (Figure 4B). But, the annual mean values are largely overestimated
459 by 30-50 micron (Figure 4D) relative to STC-MODSCAG. The seasonal distribution of region-
460 segregated SGS values from WRF-HR also compares well with that from STC-MODSCAG
461 retrievals (Figure 4E and 4F). Simulated annual mean SGS from WRF-CR (Figure 4C) lack the
462 fine spatial variability seen in STC-MODSCAG and WRF-HR. Moreover, the SGS estimates are
463 largely underestimated (by up to 100 microns) by WRF-CR specifically over grids in central and



464 eastern Himalayas, TP and Kunlun ranges (Figure 4D). The large underestimation of SGS from
465 WRF-CR and overestimation of SGS from WRF-HR is present for both summer and winter
466 months (not shown). The overestimation of SGS from WRF-HR values corroborate well with the
467 finding that the simulated fSCA distribution from WRF-HR is largely skewed towards higher
468 values (Figure 3). Similarly, the unrealistically low mean values of SGS from WRF-CR over
469 Himalayas, TP and Kunlun ranges are consistent with the underestimation of fSCA and NSD
470 values over these regions (Figure 2 and 3). While, SGS retrievals from STC-MODSCAG are
471 based on observed surface reflectance, the modeled SGS is calculated from simulated snow mass
472 in top model layer in the grid. Hence, improvement in simulation of fSCA and NSD in high
473 resolution WRF-HR runs also caused the SGS values from WRF-HR to be closer to STC-
474 MODSCAG retrievals than SGS from WRF-CR runs. It is worth noting that the presence of
475 cloud cover influences STC-MODSCAG retrievals of SGS towards smaller grain sizes if clouds
476 are misidentified as snow. This systematic error could also contribute to the SGS differences
477 between WRF-HR and STC-MODSCAG estimates.

478

479



480

481 Figure 4: Spatial distribution of annual mean snow cover fraction (fSCA) during midday (1000-
 482 1400 LT) for water year 2013-14 from A) STC-MODSCAG retrievals and simulated values
 483 from B) WRF-HR and C) WRF-CR runs is shown. Panel D illustrates the distribution of midday
 484 mean fSCA over each subregion identified by glacier classification following Randolph Glacier
 485 Inventory. The circle and vertical legs represent mean \pm standard deviation over each region for
 486 the entire year. Here, Hindu Kush, Karakoram, W.Himalayas, C.Himalayas, E.Himalayas,
 487 Tibetan Plateau, West Kunlun and East Kunlun regions are abbreviated as HK, KK, WH, CH,
 488 EH, TP, WKun and EKun, respectively. Panel E shows time-series of daily midday SGS (hashed
 489 lines) and fSCA (solid lines) from MODSCAG (black), WRF-HR (blue) and WRF-CR (red)
 490 over a grid located near the Chotta Shingri glacier (marked by magenta diamond in Figure 3A) of
 491 western Himalaya region.

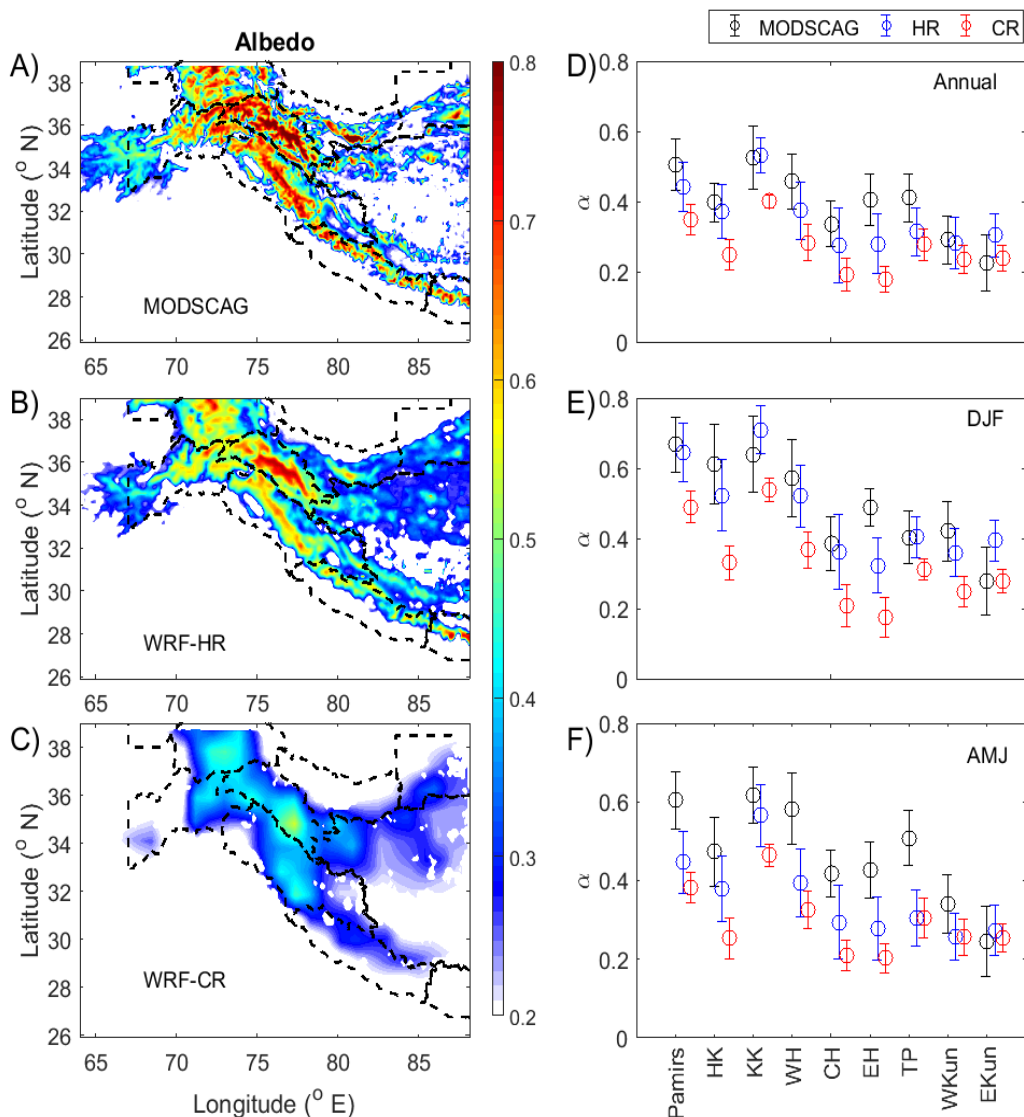


492 Interestingly, the SGS values from WRF-CR, over grids comprising the Chotta Shingri
493 glacier (marked by magenta diamond in Figure 4A) of western Himalaya, are closer to STC-
494 MODSCAG observations compared to those from the high resolution model, WRF-HR. As a
495 sanity check of the above explanation of fSCA-SGS association, daily changes of SGS (hashed
496 lines in Figure 4E) and fSCA (solid lines in Figure 4E) from STC-MODSCAG (black), WRF-
497 HR (blue) and WRF-CR (red) over this glacier are compared. Fractional snow cover from STC-
498 MODSCAG gradually increase (from below 0.2) in November, 13 (to above 0.8) in February
499 and subsequently decrease back to 0.1 gradually by Septmeber, 14 at the glacier location.
500 Corresponding SGS values from STC-MODSCAG closely followed the seasonal trend in fSCA
501 varying around the values of 80-200 micron in winter. In comparison, simulated fSCA from
502 WRF-HR values drastically increased to 1 in starting of November, 13 (from no snow cover
503 before that), remain fully snow covered till mid-June, 14 and then steeply become snow free for
504 rest of period after June. Compared to satellite estimates, fSCA from WRF-HR are greater in
505 magnitude throughout the duration of snow cover indicating more snow mass simulated by
506 WRF-HR. Associated SGS values simulated by WRF-HR values are also greater in magnitude
507 (80-800 micron) than STC-MODSCAG estimates throughout the snow duration over the grid. In
508 addition, the day to day variation in simulated SGS values is much larger than the STC-
509 MODSCAG observations. However, fSCA variation from WRF-CR over this grid is very close
510 to the variation seen by STC-MODSCAG and the associated SGS values from WRF-CR of (50-
511 400 micron) are also closer to the estimated STC-MODSCAG values, supporting our argument
512 of fSCA-linked bias in SGS estimates between model and satellite retrievals.

513 The annual mean snow albedo (α) values and the distribution over each sub region from
514 satellite estimates (by combing grain sizes from STC-MODSCAG and decrease in albedo from



515 STC-MODDRFS (see Bair et al, 2016)) and simulated by both models are presented in Figure 4.
516 Highest annual mean α values (~ 0.65 - 0.75) are observed over mountain peaks in Karakoram,
517 Pamirs and W.Himalaya regions (Figure 5A). The location and magnitude of annual mean α over
518 these grids are closely reproduced in WRF-HR with an underestimation of $< 10\%$ (Figure 5B).
519 WRF-CR simulated annual mean α values over these grids have a considerably larger
520 underestimate of $\sim 50\%$ (Figure 5C). Similar statistics are prevalent over all the sub regions of
521 HMA (Figure 5D). Specifically, the distribution of α values from WRF-HR nearly matches the
522 observed distribution, but, the distribution of albedos from the coarser model, WRF-CR, are
523 generally 0.2-0.3 lower when compared to the observations. As above, cloud misidentified as
524 snow could increase grain sized leading to slightly higher albedos. Also, note the opposite bias
525 direction for albedo simulated by WRF-HR compared to simulated SGS values. This is intuitive
526 as smaller snow particles cover greater surface area and therefore reflect more solar radiation
527 from the surface. A similar pattern in distribution of snow albedo from WRF-HR and WRF-CR
528 are also found over the sub regions for summer and winter months, separately (Figures 5E and
529 5F), indicating robust improvement in simulation of albedo values from WRF-HR throughout the
530 year. The differences in simulated α in WRF-HR with the observations increased during summer
531 and were lower during winter. Here, it is worth mentioning that we are comparing instantaneous
532 estimates obtained from Terra overpass during 1000 LT with midday (1000-1400 LT) mean
533 model values. The inherent diurnally in $-\alpha$ values under clear sky conditions in summer season
534 (Bair et al., 2017) might contribute partially to the observed enhancement in differences during
535 summer season. The improvement in α estimation from WRF-HR compared to WRF-CR can be
536 attributed to the relatively better simulation of the overall macro- and microphysical properties of
537 the snowpack in high resolution runs.



538
 539 Figure 5: Spatial distribution of annual mean snow cover fraction (fSCA) during midday (1000-
 540 1400 LT) for water year 2013-14 from A) STC-MODSCAG retrievals and simulated values from
 541 B) WRF-HR and C) WRF-CR runs is shown. Panels D-F illustrate the distribution of midday
 542 mean fSCA over each subregion identified by glacier classification following Randolph Glacier
 543 Inventory. The circle and vertical legs represent mean±standard deviation over each region for
 544 D) entire year, E) winter (December - February) and F) summer (April - June) season, separately.
 545 Here, Hindu Kush, Karakoram, W.Himalayas, C.Himalayas, E.Himalayas, Tibetan Plateau, West
 546 Kunlun and East Kunlun regions are abbreviated as HK, KK, WH, CH, EH, TP, WKun and
 547 EKun, respectively.

548



549 3.2: Aerosol distribution and LAP in snow

550 We used available in-situ and ground sun photometer measurements from seven different
551 sites across our study domain (location shown in Figure 6) to evaluate the simulated aerosol
552 optical depth (AOD). The annual mean midday AOD at each site is shown in Figure 6A. Three
553 sites (i.e. Merak, CAS and Kathmandu shown in Figures 6B-D) are located on the Himalaya
554 slopes and the other four sites (Lahore, Jaipur, Kanpur and Gandhi College shown in Figures 6E-
555 H) are located in the Indo-Gangetic Plains. In-situ measurements clearly illustrate a sharp
556 decrease (4-5 fold) in mean AOD as we traverse higher up the Himalayan slope. The annual
557 mean AOD for Lahore and Kanpur sites are 0.41 and 0.52, respectively, while the AOD over
558 high elevated sites i.e. Merak and CAS sites are 0.07 and 0.05, respectively. Also, MODIS-
559 observed AOD values prominently show the reduction in annual mean AOD from the Indo-
560 Gangetic Plains (MODIS-AOD ~ 0.4-0.7) to the Tibet region (MODIS-AOD ~ 0.1-0.2) (Figure
561 S5). Over the four sites in the Indo-Gangetic Plains, AOD simulated by both WRF-HR and
562 WRF-CR runs are well correlated with observations ($r=0.5-0.6$, Figures 6E-6H). The biases in
563 modelled AOD are also similar (in the range of 0.2-0.4) in case of both WRF-HR and WRF-CR
564 runs (Figures 6E-6H). Thus, no significant improvement in AOD values are achieved over the
565 plain region with fine resolution. However, distinct and large improvement in simulated AOD is
566 seen over the high elevation sites due to the increase in spatial resolution. Note that AOD values
567 from WRF-CR are not strongly correlated with observations at these sites (Figures 6B-6D) and
568 also have very high positive biases in AOD values (even higher than annual mean values at
569 Merak and CAS stations). In contrast, the correlation between observations and WRF-HR is
570 reasonably good ($r=0.5-0.8$ at these sites) using fine spatial resolution in WRF-HR. The positive
571 biases in AOD from WRF-HR at Merak and CAS sites are lower than corresponding WRF-CR



572 values by an order of magnitude. Presence of lower biases in AOD from WRF-HR over high
573 elevation sites indicates that the observed sharp decrease in AOD values across the Himalayan
574 slope are better captured by the higher resolution WRF run (WRF-HR) than in the coarser run.
575 Greater annual mean AOD value is simulated by WRF-CR over the entire HMA region
576 compared to WRF-HR (Figure S5) supporting an overestimation of AOD from WRF-CR at
577 higher elevation in addition to the few sites. The presence of high biases (0.3-0.4) over
578 Kathmandu valley even in WRF-HR runs indicate that model resolution even finer than 12 km is
579 likely needed to better resolve the AOD distribution in complex terrain around valleys in
580 Himalayan slope regions. Moreover, Jayarathne et al., 2018 shows that many local emissions are
581 not accounted in global emissions which causes underestimation in simulated regional AOD
582 values in these valleys. Temporal variability in monthly mean AOD (relatively higher AOD in
583 summer) is simulated reasonably well by both the model versions (Figure S5).

584

585

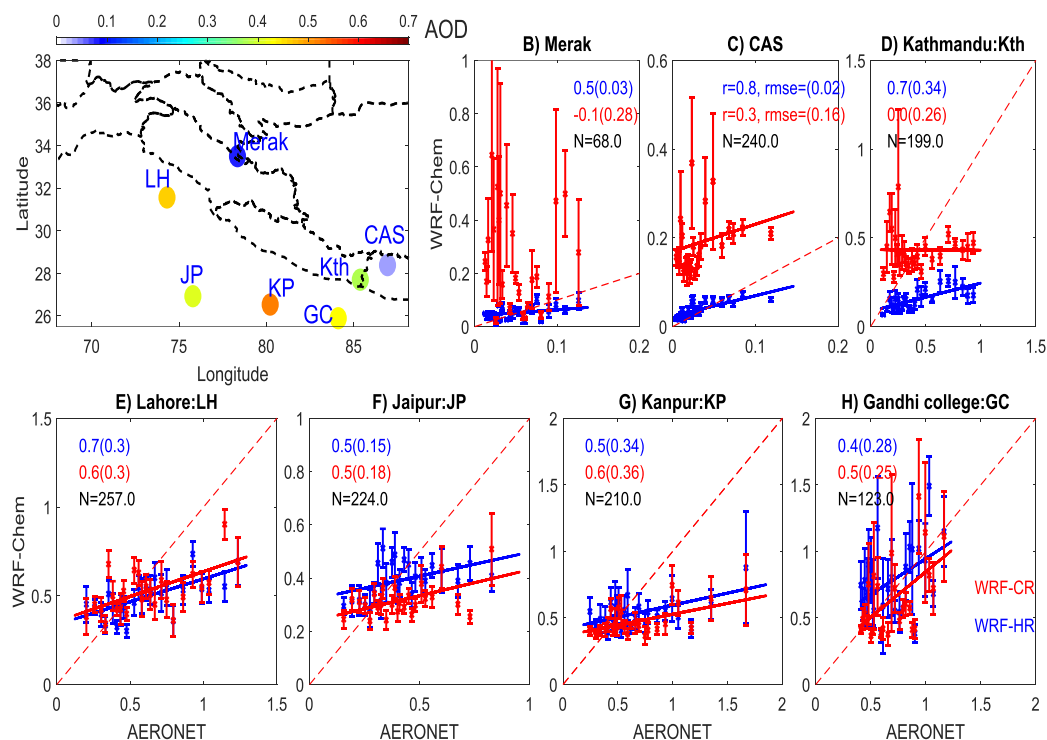
586

587

588

589

590



591

592 Figure 6: Comparison of midday (averaged over 1000-1400 LT) aerosol optical depth (AOD)
 593 measured by ground based sun photometer at seven sites within the study domain with
 594 corresponding simulated AOD values from, both, WRF-HR and WRF-CR. The annual mean
 595 AOD values over each site is shown by shade in topmost left Panel. The other panels illustrates
 596 the comparison over one of each stations shown by dots in topmost left Panel. The 'N'
 597 mentioned in the legend in each panel is the total number of days when collocated data between
 598 model and measurement is available over that site. These sample points are divided into 50 equal
 599 bins of ascending AERONET-AOD values (2 percentile each) and averaged. The standard
 600 deviation in each bin is shown by the vertical bars. The correlation coefficient values (r) are also
 601 mentioned in the legend followed in brackets by the relative error values ($\sum \text{rmse}/\text{mean obs}$).

602

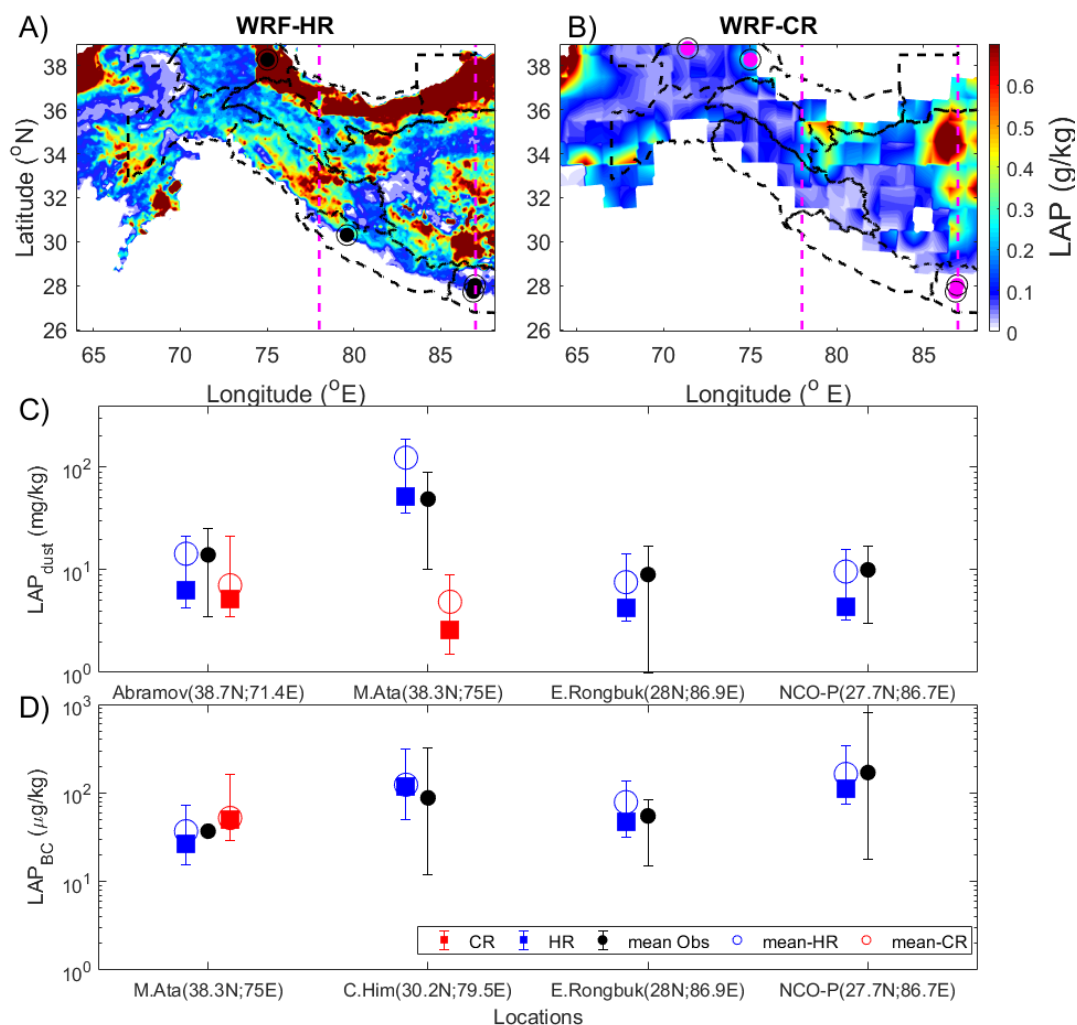
603

604

605



606



607

608 Figure 7: Spatial distribution of annual mean LAP concentration in snow top layer for water year
 609 2013-14 simulated by A) WRF-HR and B) WRF-CR. The black dots in Panel A denote the
 610 locations where observations of BC in snow is available. Similarly, the magenta dots in Panel B
 611 denote the locations from where observation of dust in snow is available. Panels C-D illustrate
 612 comparison of simulated LAP_{BC} (top) and LAP_{dust} (bottom), respectively, in topmost snow layer
 613 with observed values over the marked locations in the Himalayan cryosphere. Annual mean
 614 (circle) and distribution (box plot) is used as metric of comparison. The WRF-HR and WRF-CR
 615 values are represented by blue and red, respectively. The pink lines in Panel A are the cross-
 616 sections shown in Figure 8.

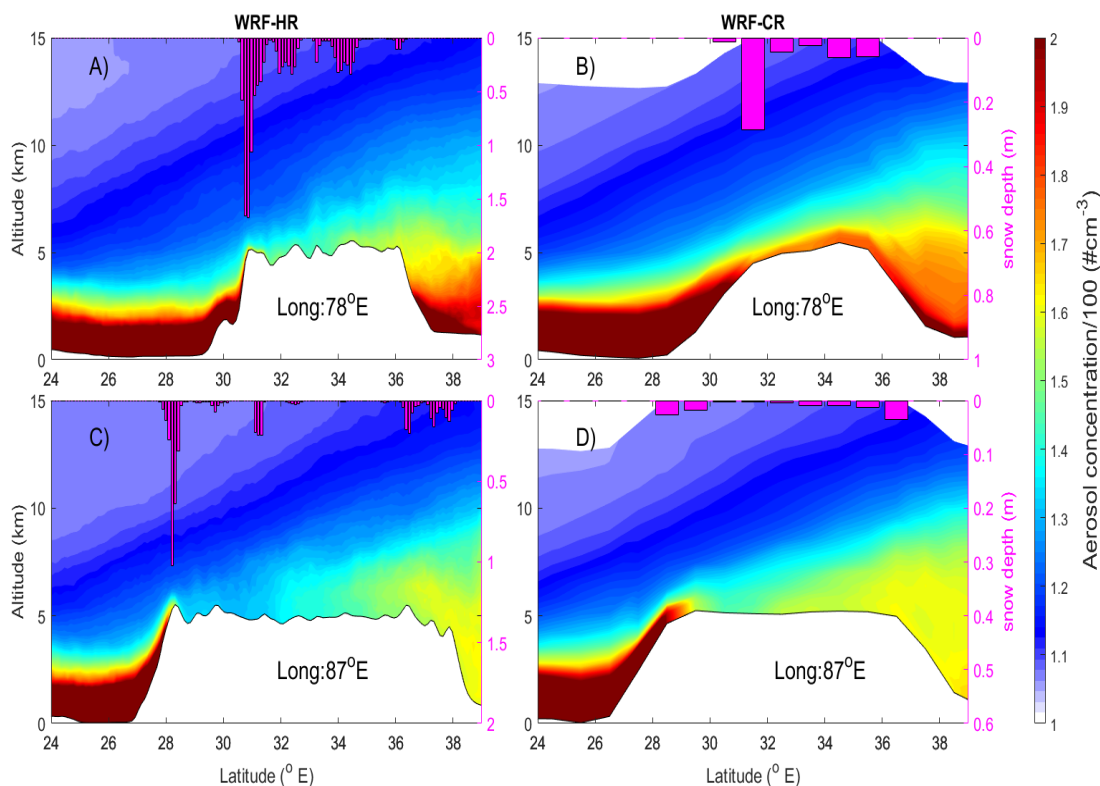


617 Significant differences in simulated AOD over high elevations of Himalaya slopes and
618 TP indicate that considerable differences might also be present in LAP concentrations in snow
619 between the two WRF simulations. Annual mean LAP concentrations in top snow layer from
620 WRF-HR and WRF-CR simulations are compared in Figures 7A-7B. The comparison shows that
621 LAP concentration in WRF-HR are significantly higher than WRF-CR simulated values.
622 Quantitatively, the WRF-HR simulated annual mean LAP concentrations over the Pamir (0.5
623 g/kg), Karakoram (0.45 g/kg), Hindu Kush (0.2 g/kg), W. Himalaya (0.3 g/kg), C. Himalaya (0.2
624 g/kg) and E. Himalaya (0.08 g/kg) ranges is 3-5 times higher than the same from WRF-CR runs.
625 In contrast, WRF-HR simulated LAP over TP (0.21 g/kg) and Kunlun ranges (0.8 g/kg) is similar
626 to the mean magnitude simulated by WRF-CR runs. As a sanity check, we evaluate the simulated
627 LAP concentrations against those previously reported in the literature. Figures 7C and 7D
628 illustrate the evaluation of mean annual LAP concentration from WRF-HR and WRF-CR
629 associated with BC (LAP_{BC}) and dust (LAP_{dust}), respectively, against the reported data (shown as
630 filled black circles). The locations of reported LAP_{BC} (black filled dots) and LAP_{dust} (magenta
631 filled dots) are shown in Figure 7C and Figure 7D, respectively. First, the difference in the
632 magnitude of LAP_{dust} and LAP_{BC} over HMA is striking. The LAP_{dust} is more than 1000 times
633 greater than LAP_{BC} both in observations and the models. Secondly, LAP_{BC} and LAP_{dust} values
634 from WRF-HR are much closer to reported values compared to WRF-CR values. The differences
635 in mean of reported LAP_{BC} and LAP_{dust} distribution to that simulated by WRF-HR at various
636 sites are in range of 5-30 $\mu\text{g}/\text{kg}$ and 5-20 mg/kg , respectively. WRF-CR well simulates the
637 concentrations of LAP_{BC} and LAP_{dust} over Pamirs ($\sim 10 \text{ mg}/\text{kg}$), but significantly underestimates
638 the LAP_{BC} and LAP_{dust} (by an order of magnitude) over the Himalayan ranges. Although the
639 reported data are not specific to water year 2013-14, it can be reasonably assumed that the inter-



640 annual variations of LAP concentration in snow is of the order of magnitude as uncertainty in the
641 observations. Thus, the WRF-HR better simulates aerosol and LAP concentration than the WRF-
642 CR over the HMA region.

643 It is interesting to note that finer spatial resolution resulted in lower AOD but greater
644 LAP values in snow over some places in HMA. For more insight, the vertical distribution of
645 aerosol concentration in altitude-latitude space (Figure 8) across two latitudinal cross-sections
646 (magenta colored lines in Figure 7A) is analyzed. Figure 8 illustrates the differences in simulated
647 vertical distribution of mean aerosol number concentration along 78°E (row 1) and 87°E (row 2)
648 for WRF-HR (left column) and WRF-CR (right column) runs, respectively. Corresponding
649 terrain elevation (black solid line) and snow depth (magenta bars) are also overlaid in these plots.
650 The latitude-altitude plots clearly illustrate that improved representation of the terrain in WRF-
651 HR shows the sharp change of elevation over Himalayan foothills and causes a steeper natural
652 barrier to the transport of aerosols uphill from IGP to HMA region than in the WRF-CR model.
653 Also, high spatial resolution enhances snowfall in WRF-HR over the HMA region relative to the
654 WRF-CR model. While the former change increased annual dry deposition flux, more snowfall
655 caused greater wet deposition annually in WRF-HR compared to WRF-CR (Figure S6). The
656 combination of these effects increases the deposition of aerosols and therefore LAP on the
657 southern slopes of Himalaya in the WRF-HR run. This explains the coexistence of higher LAP
658 concentration/deposition and lower AOD across HMA in WRF-HR, compared to corresponding
659 WRF-CR results.



660

661 Figure 8: Longitudinally-averaged annual mean aerosol number concentration plotted in altitude-
662 latitude space for two longitudinal traverses across the study domain, i.e. 78°N (Panels A and B)
663 and 87°N (Panels C and D) for both WRF-HR (left column) and WRF-CR (right column).

664 Corresponding terrain elevation is shown in solid black line. Corresponding to each latitude, the
665 longitudinally-averaged annual mean snow depth is also presented in magenta color bars (using
666 y-axis on the right).

667

668

669

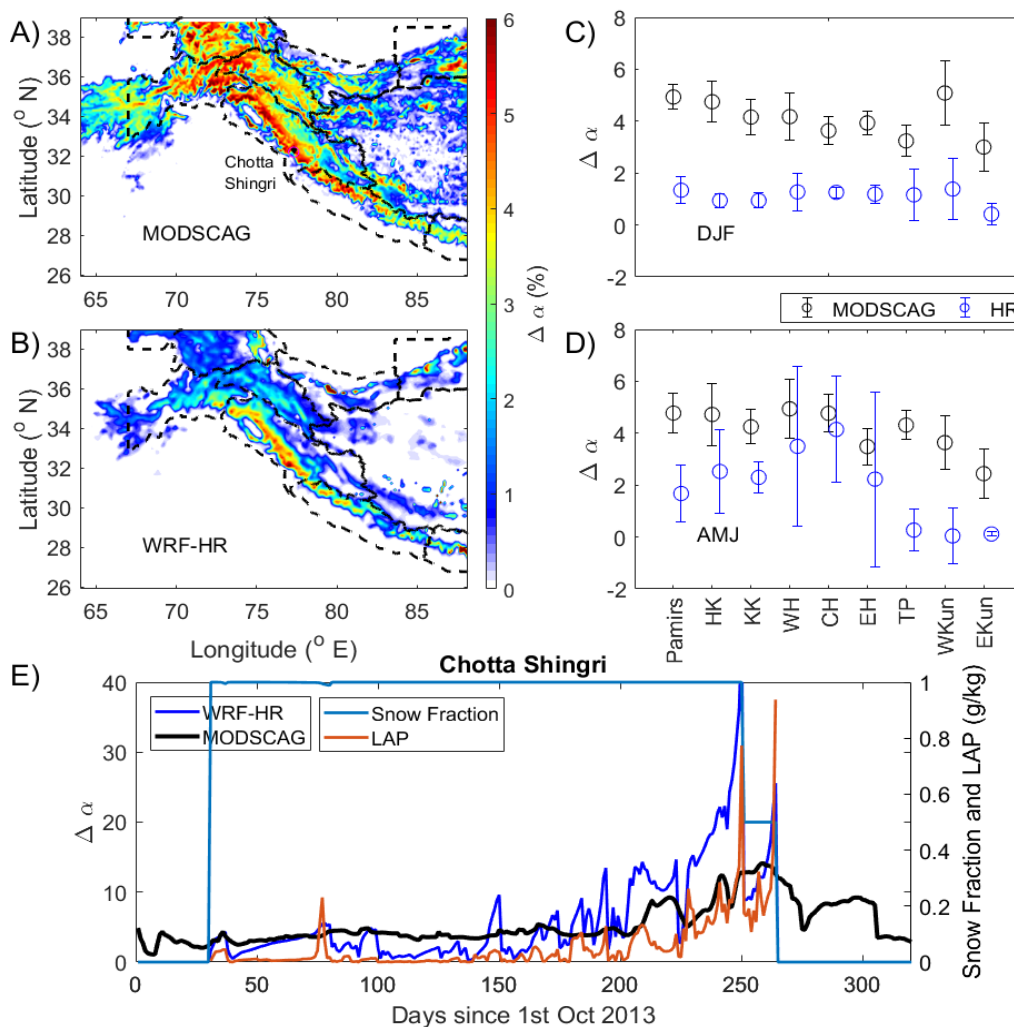
670

671

672



673 **3.3 LAP-induced Snow darkening and radiative forcing**



674
 675 Figure 9: Spatial distribution of annual mean LAP-induced snow albedo darkening ($\Delta\alpha$) during
 676 midday (1000-1400 LT) for water year 2013-14 from A) MODSCAG retrievals and B) simulated
 677 values from WRF-HR is shown. Panels C and D illustrate the distribution of midday mean $\Delta\alpha$
 678 over each sub region identified by glacier classification following Randolph Glacier Inventory.
 679 The circle and vertical legs represent mean \pm standard deviation over each region for entire year.
 680 Here, Hindu Kush, Karakoram, W.Himalayas, C.Himalayas, E.Himalayas, Tibetan Plateau, West
 681 Kunlun and East Kunlun regions are abbreviated as HK, KK, WH, CH, EH, TP, WKun and
 682 EKun, respectively. Panel E shows time-series of daily midday $\Delta\alpha$ from STC-MODSCAG
 683 (black) and WRF-HR (blue) over the grids located near the Chotta Shingri glacier (marked in
 684 Figure A) of western Himalaya region. Also fractional snow cover and LAP concentrations from
 685 WRF-HR over the same grids are included.



686

687 STC-MODDRFS retrievals illustrate that locations in Hindu Kush and W. Himalayas
688 have the highest annual mean LAP-induced reduction in snow albedo ($\Delta\alpha$ in %) followed by
689 Karakoram, C.Himalayas and Pamir regions (Figure 9A). WRF-HR simulated the spatial
690 variations in annual mean $\Delta\alpha$ reasonably well (Figure 9B), but, the magnitudes are
691 underestimated by ~20-40 % throughout the domain. Note that the biases in annual mean values
692 are lowest over grids in Himalayan ranges (where the underestimation is within 20%). Season
693 wise and region wise distribution plots show that the WRF-HR biases are higher in winter
694 months than the summer months (Figures 9C and 9D). While, WRF-HR simulated $\Delta\alpha$ values in
695 the winter span between 1-3 %, the corresponding STC-MODDRFS estimates of $\Delta\alpha$ are larger
696 with values ranging between 3-6% (thus no overlap with model values) over all the sub regions.
697 In summer months, the distribution of modeled WRF-HR $\Delta\alpha$ values over Karakoram and
698 Himalayan ranges are similar in magnitude, explaining the lower biases in annual mean values
699 over Himalayas. This spatiotemporal variability in differences between STC-MODDRFS
700 retrievals and simulated $\Delta\alpha$ values is consistent with the variability in biases of fractional snow
701 cover seen in WRF-HR (Figures 2E and 2F). Specifically, the large underestimation [and
702 significant improvement relative to WRF-CR] in WRF-HR- $\Delta\alpha$ values (Figures 9C and 9D) in
703 winter [summer] over Karakoram, Hindu Kush and Himalayas is in agreement with
704 corresponding overestimation [improvement] of fSCA from WRF-HR over these regions (Figure
705 2).

706 For a closer look, the difference in daily midday mean $\Delta\alpha$ values from STC-MODDRFS
707 (black) and WRF-HR (blue) are compared (in Figure 9E) over the grids of Chotta Shingri glacier
708 (similar as Figure 4E). Corresponding, midday mean fSCA (light blue) and LAP (orange) from



709 WRF-HR are also plotted. $\Delta\alpha$ values from STC-MODDRFS are about 5% during winter months,
710 but, increases in summer months until mid-June (peak value is 18%). Albedo reduction is closely
711 associated with the temporal progression in midday LAP concentration in snow over this region
712 at daily scale. In agreement, midday $\Delta\alpha$ values from WRF-HR are lower in winter months and
713 higher in summer months. Except occasional peaks, with magnitudes of 3-4 %, $\Delta\alpha$ values from
714 WRF-HR largely remained below 3 % till late February. A steep increase in $\Delta\alpha$ values from
715 WRF-HR is seen in March (monthly mean \sim 4%), April (9%), May (13%) and June (18%). As
716 already discussed, the simulated fSCA values in WRF-HR are greater than observed fSCA from
717 STC-MODSCAG for most of the winter season (Figure 4E). STC-MODDRFS estimated $\Delta\alpha$ is
718 based on surface reflectance, while $\Delta\alpha$ calculated by model is for a surface layer of \sim 3 cm. The
719 surface snow layer in SNICAR/CLM continuously evolves as fresh snowfall is added or with
720 snow melting, so the LAP concentrations in surface layer depend on new snowfall, meltwater
721 flushing, and layer combination/division (Flanner et al., 2007; Flanner et al., 2012; Oleson et al.,
722 2010). Thus, more snow cover or thicker surface layers in winter results in lower values of
723 annual mean LAP concentration and thus underestimates associated with LAP-induced snow
724 darkening. In addition, the associated overestimation in modelled SGS during winter (Figure 4E)
725 can also contribute to the lower WRF-HR- $\Delta\alpha$ values, because, bigger snow grains in WRF-HR
726 lead to lower clean albedo and thus smaller reduction in albedo compared to STC-MODDRFS .

727 Another notable point is the large $\Delta\alpha$ values ($>$ 20 %) from WRF-HR that occur towards
728 the end of snow cover in June, which, is not seen in the STC-MODDRFS retrievals. The
729 variations could be due to 2 reasons, either the snowpack is underestimated or the LAP
730 concentration is overestimated by the model. Some factors which can contribute to these
731 discrepancies in summer are 1) Larger LAP values may be simulated due to model uncertainties



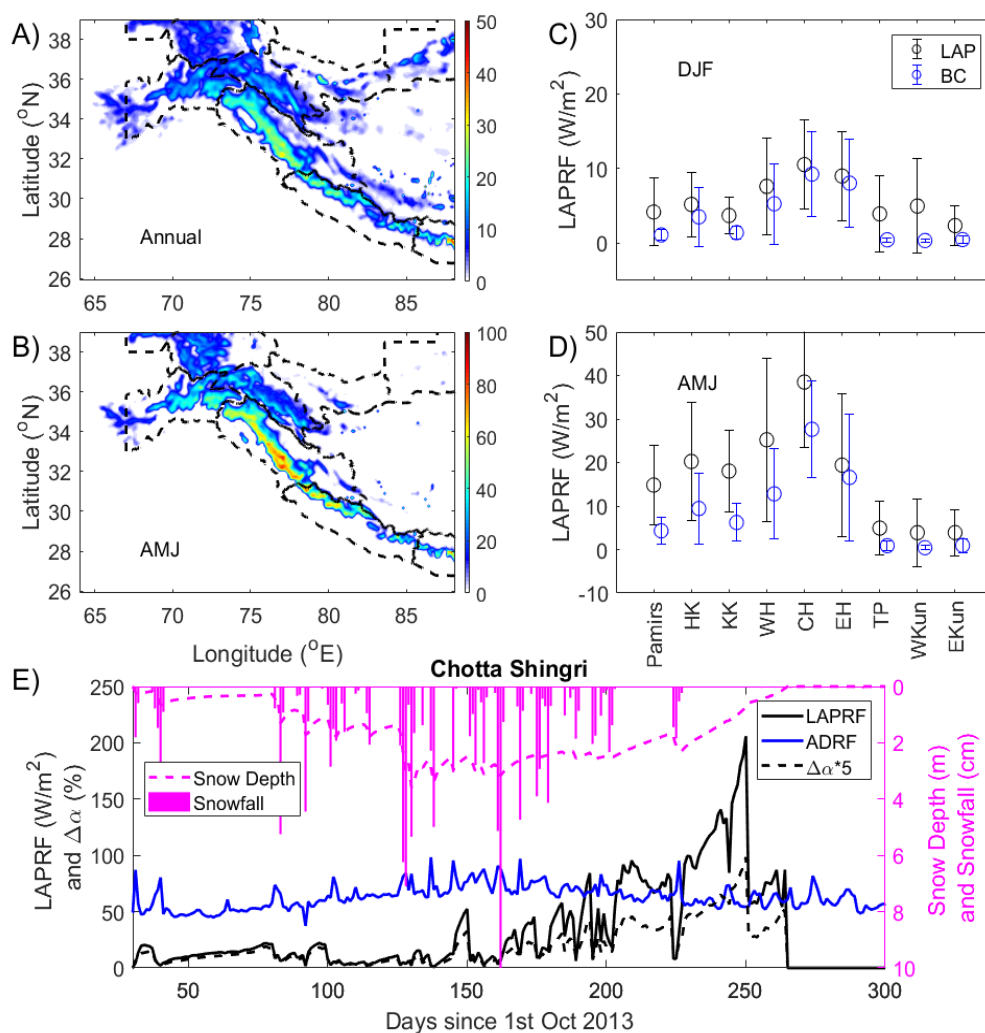
732 in enhanced wet scavenging fluxes; 2) It is well known that with transport and deposition of
733 aerosols from IGP to W.Himalayas increases afternoon with evolution of boundary layer over the
734 IGP region (Dumka et al., 2015; Raatikainen et al., 2014). This feature is well simulated by the
735 model (not shown). As STC-MODDRFS estimates are representative of 1000 LT, but, modelled
736 values are representative of midday mean (1000-1400 LT), more aerosol deposition might be
737 resulting in higher $\Delta\alpha$ values WRF-HR during summer months; 3) At the same time, the
738 uncertainties associated with modelling aerosol-snow albedo microphysical feedbacks to snow
739 melt may also be contributing to underestimation of snow packs in summer. However, more
740 certainty on these modelled values require evaluation against in-situ measurements. It is worth
741 mentioning here that no in-situ measurements are available for direct comparison of these high
742 $\Delta\alpha$ values WRF-HR over W.Himalayas (Gertler et al., 2016). Nonetheless, the high values
743 simulated during summer end are in near-range of previously reported values over other HMA
744 regions. Kaspari et al., (2014) used the offline SNICAR model to report that BC concentrations
745 in spring snow/ice samples at Mera Glacier were large enough to reduce albedo by 6-10% but
746 that with the inclusion of dust, the reduction in albedo was 40-42% relative to clean snow.
747 Recently, Zhang et al., 2018 has combined a large dataset of LAP measurements in surface snow
748 with offline SNICAR model to illustrate that $\Delta\alpha$ can be >35% over Tibetan Plateau. Moreover,
749 the composite effect of this discrepancy on seasonal/annual mean values is minimal as the
750 snowpack is at its minimum at summer end. Similar high daily variability and huge LAPRF
751 values (~ 200 W/m²) in late summer as well as associated sudden decline in snow depth is also
752 reported in sites over upper Colorado river basin (Skiles et al., 2015; Skiles and Painter, 2017).

753

754



755



756
 757 Figure 10: A) Spatial distribution of annual mean snow mediated LAP-induced radiative forcing
 758 (LAPRF) from WRF-HR and B) Spatial distribution of seasonal mean LAPRF over snow
 759 covered for summer season (AMJ) of water year 2013-14. Panels C and D illustrate the
 760 distribution of LAPRF (blue) and BC-only-LAPRF (black) over each sub region identified by
 761 glacier classification following Randolph Glacier Inventory for winter and summer, respectively.
 762 The circle and vertical legs represent mean±standard deviation over each region for entire year.
 763 Here, Hindu Kush, Karakoram, W.Himalayas, C.Himalayas, E.Himalayas, Tibetan Plateau, West
 764 Kunlun and East Kunlun regions are abbreviated as HK, KK, WH, CH, EH, TP, W.Kun and
 765 E.Kun, respectively. Panel E shows time-series of daily midday LAPRF (blue) and aerosol direct
 766 radiative forcing at surface (ADRF, blue) over the Chotta Shingri region (marked in Figure 9A)
 767 of western Himalayan region. The simulated LAP-induced change in snow albedo is also shown



768 in hashed black line. Also snow depth and snowfall from WRF-HR over the same grid is
769 included.

770 In agreement with the spatial variation in $\Delta\alpha$ values, the annual mean snow-mediated
771 LAP-induced radiative forcing (LAPRF) from WRF-HR over grids in W.Himalayas and C.
772 Himalayas are highest followed by Karakoram, Hindu Kush, E.Himalayas and Pamir regions
773 (Figure 10A). The spatial distribution of summer mean LAPRF values from WRF-HR (Figure
774 10B) is similar to that of the annual mean LAPRF values, but, the summer magnitudes are higher
775 by an order of magnitude throughout most of the domain. This is mainly due to the large increase
776 in $\Delta\alpha$ values in summer when LAPs aggregate on the surface compared with winter months
777 when LAPs are continuously covered by new snow (Figure 9). Spatio-temporal variability in
778 LAPRF is evident in the seasonal and regional distribution plots (Figure 10C and 10D). LAPRF
779 values over the edges of HMA are greater than the highland TP region in both winter and
780 summer months probably due to greater LAP deposition simulated over Hindu Kush, Karakoram
781 and Himalayas regions (Figure S7) from the close proximity of dust sources. Also, it is clearly
782 visible that the maximum LAPRF values within HMA region are present over grids in
783 Himalayan ranges (during both winter and summer) with annual mean values $> 50 \text{ W/m}^2$ (seen in
784 Figures 10B and 10D) and maximum instantaneous values higher than 150 W/m^2 (not shown).

785 The time series of midday mean LAPRF values (Figure 10E) over the same grids in the Chotta
786 Shingri Glacier region in western Himalaya is plotted to ascertain possible daily variability in
787 LAPRF for midday over the region. Corresponding LAP-induced albedo reduction, snow depth
788 and snowfall values are also plotted to show how LAPRF can affect local snow melting. The
789 daily snow depth increases to 3.6 m in winter (30-150 days) followed by gradual reduction and
790 snow cover melting in summer (150-270 days). The mean midday LAPRF value is $\sim 10 \text{ W/m}^2$ in
791 winter season, but, the magnitude increased gradually during March (18 W/m^2), April (44



792 W/m^2), May (86 W/m^2) and June (123.5 W/m^2), eventually terminating with a peak value of 202
793 W/m^2 in mid-June. The temporal evolution in $\Delta\alpha$ values closely followed the LAPRF values with
794 a variation in range of 1-20%. The shortwave aerosol direct radiative forcing (ADRF) during
795 midday at the surface over the same grid is also shown (as blue curve) in Figure10E. The
796 momentarily high values of ADRF during the period indicate dust storms or sudden increase in
797 aerosol loading over the grid. A closer look illustrate that the large daily variations in LAPRF
798 and $\Delta\alpha$ are associated with the variability in ADRF and daily snowfall occurrence over the grid.
799 Fresh snowfall feedbacks result in subsequent reduction in LAPRF and enhancement in snow
800 depth (Figure10E), while, higher aerosol loading over aged snow is followed by a clear increase
801 in LAPRF. During melting, our model considers that only a fraction of LAP is washed away with
802 meltwater, which, results in enhanced concentration of LAP during the end stages of the
803 snowpack. This snow albedo feedback along with the momentary high aerosol loading (on 250th
804 day) can explain the very high values of albedo reduction and LAPRF that were simulated during
805 the last days of the snow cover over this grid. Higher LAPRF values indicate more energy being
806 absorbed by the snow pack and thus more snow melting. Therefore, LAP-induced snow melting
807 effect over Himalaya is very significant and is the largest relative to other areas within HMA.

808 Snow-mediated radiative forcing only due to BC- deposition is shown in Figures10C and
809 10D. Although, similar spatiotemporal pattern in LAPRF and BC-only-LAPRF is simulated,
810 contrasting features in context to BC contribution to LAPRF are present in between the western
811 part and eastern parts of HMA. During winter, the magnitude of BC-only LAPRF values is
812 similar to that of total LAPRF over the western part of HMA region (i.e. Pamirs, Karakoram,
813 Hindu Kush and W.Himalayas) suggesting that BC is a dominant contributor to net LAPRF
814 (Figures10C). But, large differences between LAPRF and BC-only LAPRF is present during



815 summer season over the western regions indicating that dust contribution is more or less equal to
816 that of BC contribution over these regions (Figure10D). In contrast, the dust contribution to
817 LAPRF values over the eastern domain (TP and Kunlun regions) is significant during winter
818 season (Figures10C and 10D). The spatiotemporal variability in dust and BC contribution is
819 reported previously and is mainly linked with the seasonal variability in meteorology and
820 associated advection of South Asian emissions (Zhang et al., 2015; Wang et al., 2015a ; Niu et
821 al., 2018). The ADRF-induced surface cooling effect may nullify the effects of LAPRF-induced
822 warming effect on snowpack melting. But, the drastic increase in LAPRF values in April through
823 June causes the magnitude of LAPRF to be twice that of ADRF over W. Himalayas during snow
824 melting period, highlighting dominance of LAPRF (as also seen in Figure10E).

825 The simulated annual mean, summer mean and BC-only-LAPRF values from WRF-HR
826 are in general, higher compared to previously reported estimates of LAPRF from model studies
827 at coarser resolution. For example, Ménégos et al., (2014) have reported annual mean LAPRF of
828 $\sim 1\text{-}3\text{ W/m}^2$ over Himalaya using an online simulation at 50 km resolution grid. Similarly, Qian
829 et al., (2011) used the Community Atmosphere Model version 3.1 at coarser spatial resolution to
830 show that simulated aerosol-induced snow albedo perturbations can generate LAPRF values of
831 $5\text{-}25\text{ W/m}^2$ during spring over HMA. Also, coarsely resolved GEOS-Chem runs simulated BC-
832 only-LAPRF can vary from 5 to 15 W/m^2 in the snow-covered regions over the TP (Kopacz et
833 al., 2011). Recently, a decade long simulation using the RegCM model at 50 km spatial
834 resolution also estimated maximum BC-only-LAPRF values of $5\text{-}6\text{ W/m}^2$ over the Himalaya and
835 southeastern TP averaged over non-monsoon season (Ji, 2016). However, the comparison of
836 WRF-HR and WRF-CR simulations provided in this study clearly show that the magnitudes of
837 snow macro- and micro-properties, aerosol loading and LAP-induced albedo darkening over



838 Himalayas improved significantly with finer spatial resolution. Thus, the global model simulated
839 LAPRF values are likely underestimated. In agreement, recently, Zhang et al., (2018) and has
840 estimated BC-only-LAPRF of 20-35 W/m² using offline SNICAR calculation forced with a
841 greater coverage of measurements of surface snow content. He et al., (2018) have also reported
842 similar high BC-only-LAPRF values after implementing a realistic snow grainsize
843 parameterizations in offline SNICAR calculations over HMA.

844 **4. Summary and Implications**

845 In this study, we use the SNICAR model coupled with WRF-Chem regional model at high
846 spatial resolution (WRF-HR; 12 km) to simulate the transport, deposition, and radiative forcing
847 of light absorbing particles (LAPs; mainly Black Carbon and dust) over the high mountains of
848 Asia (HMA) during water year 2013-14. The snow grain sizes and LAP-induced snow darkening
849 was evaluated, for the first time, against comprehensive satellite retrievals (the MODSCAG and
850 MODDRFS spatial and temporally complete retrieved satellite observations) over HMA. The
851 atmospheric aerosol loading is evaluated against satellite and ground-based AOD measurements
852 over HMA region. Results from another simulation which employ the same model configuration
853 but a coarser spatial resolution (WRF-CR; 1 degree) are also compared with WRF-HR to
854 illustrate the significance of a better representation of terrain on snow-pack and aerosol
855 simulation over HMA. The main conclusions from our study are:

- 856a) The simulated macro- and micro-physical properties and the duration of snow packs over HMA
857 improve significantly due to the use of fine spatial resolution, especially over the southern slopes
858 of Hindu Kush and Himalayan ranges.
- 859b) Simulated aerosol loading over HMA is also more realistic in WRF-HR than in WRF-CR, which
860 leads to a reduction in biases of annual mean LAP concentration in snow. This improvement is



861 attributed to a more realistic simulation of wet deposition (due to a better simulation of snow
862 pack) and dry deposition of LAPs (associated with a better representation of terrain) in WRF-
863 HR.

864c) WRF-HR captures the magnitude of LAP-induced snow albedo reduction ($\Delta\alpha$) over Himalayas
865 and Hindu Kush region relatively well compared to the STC-MODDRFS retrievals during
866 summer. However, during winter, large biases in modelled $\Delta\alpha$ values are present. This is
867 probably due to inherent uncertainties in model parameterizations and satellite retrievals
868 associated with the cloud cover over HMA in winter period.

869d) The glaciers and snow cover regions located in the Himalaya have the highest LAPRF within
870 HMA i.e. annual mean LAPRF $\sim 20 \text{ W/m}^2$ and summer mean LAPRF $\sim 40 \text{ W/m}^2$. This is
871 consistent with similar high values of $\Delta\alpha$ over Himalayan ranges i.e. annual mean $\Delta\alpha$ values ~ 2 -
872 4 % and summer mean $\Delta\alpha$ values ~ 4 -8 %. The annual mean LAP concentration in snow values
873 (200-300 mg/kg) are also high. Thus, the Himalaya (more specifically, western Himalayas) is
874 most vulnerable to LAP-induced snow melting within HMA.

875

876 Ramanathan and G. Carmichael, (2008) suggest that atmospheric warming from LAPs
877 ($\sim 20 \text{ W/m}^2$) may be just as important as greenhouse gases in the melting of snowpack and
878 glaciers over Asia. In this context, the high magnitudes of LAPRF values in summer over HMA
879 ($\sim 40 \text{ W/m}^2$) clearly shows that snow-mediated aerosol forcing on snow melting over HMA can
880 be twofold the significance of the atmospheric forcing. Nonetheless, the differences in snow
881 surface properties between WRF-HR and satellite observations indicate probable uncertainties in
882 model parameterizations. At the same time, the STC-MODDRFS retrievals themselves may have
883 an uncertainty of $\sim 5\%$ in instantaneous $\Delta\alpha$ measurements. Thus, efforts to further reducing the



884 LAPRF uncertainties in the model are warranted in the future by using in-situ observations (i.e.
885 field campaigns), specifically over the most affected western Himalayas, where relevant
886 measurements are largely absent (Gertler et al., 2016). Moreover, satellite retrievals will be
887 markedly improved in the coming decade with the NASA Decadal Survey Surface Biology and
888 Geology imaging spectrometer mission, which includes as a core measurement snow albedo and
889 its controls (National Academies of Science, 2018). These visible through shortwave infrared
890 imaging spectrometer retrievals have uncertainties an order of magnitude smaller (Painter et al.,
891 2013) than those from multispectral sensors such as MODIS and will provide a more accurate
892 constraint on the physically-based modeling pursued here.

893

894 **Acknowledgment**

895 This research was supported by the NASA High Mountain Asia Project. The Pacific Northwest
896 National Laboratory (PNNL) is operated for DOE by Battelle Memorial Institute under contract
897 DE-AC06-76RLO 1830. Part of this work was performed at the Jet Propulsion Laboratory,
898 California Institute of Technology under contract with NASA. H. Wang acknowledges support
899 from the U.S. Department of Energy (DOE), Office of Science, Biological and Environmental
900 Research as part of the Earth System Modeling program. We thank the PIs of the selected
901 AERONET and SKYNET stations, for providing the data used in this study. The AERONET
902 data are obtained from the AERONET website, <http://aeronet.gsfc.nasa.gov/>. We also thank the
903 PI of the selected SkyNet station, for providing the data used in this study. The SkyNet data is
904 obtained from the website <http://atmos3.cr.chiba-u.jp/skyenet/merak/merak.html/>.

905

906 **References**

- 907 Amante, C. and Eakins, B. W.: ETOPO1 1 Arc-Minute Global Relief Model: Procedures, Data
908 Sources and Analysis., 2009.
- 909 Azam, M. F., Ramanathan, A., Wagnon, P., Vincent, C., Linda, A., Berthier, E., Sharma, P.,
910 Mandal, A., Angchuk, T., Singh, V. B. and Pottakkal, J. G.: Meteorological conditions, seasonal
911 and annual mass balances of Chhota Shigri Glacier, western Himalaya, India, *Ann. Glaciol.*,
912 57(71), 328–338, doi:10.3189/2016AoG71A570, 2016.
- 913 Bair, E. H., Rittger, K., Davis, R. E., Painter, T. H. and Dozier, J.: Validating reconstruction of
914 snow water equivalent in California's Sierra Nevada using measurements from the NASA
915 Airborne Snow Observatory, *Water Resour. Res.*, 52(11), 8437–8460,
916 doi:10.1002/2016WR018704, 2016.
- 917 Barnard, J. C., Fast, J. D., Paredes-Miranda, G., Arnott, W. P. and Laskin, A.: Technical note:
918 Evaluation of the WRF-Chem “Aerosol chemical to aerosol optical properties” module using
919 data from the MILAGRO campaign, *Atmos. Chem. Phys.*, 10(15), 7325–7340, doi:10.5194/acp-
920 10-7325-2010, 2010.
- 921 Barnett, T. P., Adam, J. C. and Lettenmaier, D. P.: Potential impacts of a warming climate on
922 water availability in snow-dominated regions, *Nature*, 438(7066), 303–309,
923 doi:10.1038/nature04141, 2005.
- 924 Binkowski, F. S. and Shankar, U.: The Regional Particulate Matter Model. 1. Model description
925 and preliminary results, *J. Geophys. Res.*, 100(D12), 26191–26209, doi:10.1029/95JD02093,
926 1995.
- 927 Bolch, T., Kulkarni, A., Kääb, A., Huggel, C., Paul, F., Cogley, J. G., Frey, H., Kargel, J. S.,
928 Fujita, K., Scheel, M., Bajracharya, S. and Stoffel, M.: The state and fate of himalayan glaciers,
929 *Science* (80-.), 336(6079), 310–314, doi:10.1126/science.1215828, 2012.
- 930 Bollasina, M. A., Ming, Y. and Ramaswamy, V.: Anthropogenic Aerosols and the Weakening of
931 the South Asian Summer Monsoon, *Science* (80-.), 334(6055), 502–505,
932 doi:10.1126/science.1204994, 2011.
- 933 Bonasoni, P., Laj, P., Marinoni, A., Sprenger, M., Angelini, F., Arduini, J., Bonafè, U., Calzolari,
934 F., Colombo, T., Decesari, S., Di Biagio, C., Di Sarra, A. G., Evangelisti, F., Duchi, R., Facchini,
935 M. C., Fuzzi, S., Gobbi, G. P., Maione, M., Panday, A., Roccatò, F., Sellegri, K., Venzac, H.,
936 Verza, G. P., Villani, P., Vuillermoz, E. and Cristofanelli, P.: Atmospheric Brown Clouds in the
937 Himalayas: First two years of continuous observations at the Nepal Climate Observatory-
938 Pyramid (5079 m), *Atmos. Chem. Phys.*, 10(15), 7515–7531, doi:10.5194/acp-10-7515-2010,
939 2010.
- 940 Bond, T. C., Doherty, S. J., Fahey, D. W., Forster, P. M., Berntsen, T., Deangelo, B. J., Flanner,
941 M. G., Ghan, S., Kärcher, B., Koch, D., Kinne, S., Kondo, Y., Quinn, P. K., Sarofim, M. C.,
942 Schultz, M. G., Schulz, M., Venkataraman, C., Zhang, H., Zhang, S., Bellouin, N., Guttikunda,
943 S. K., Hopke, P. K., Jacobson, M. Z., Kaiser, J. W., Klimont, Z., Lohmann, U., Schwarz, J. P.,
944 Shindell, D., Storelvmo, T., Warren, S. G. and Zender, C. S.: Bounding the role of black carbon
945 in the climate system: A scientific assessment, *J. Geophys. Res. Atmos.*, 118(11), 5380–5552,
946 doi:10.1002/jgrd.50171, 2013.



- 947 Brandt, R. E., Warren, S. G. and Clarke, A. D.: A controlled snowmaking experiment testing the
948 relation between black carbon content and reduction of snow albedo, *J. Geophys. Res. Atmos.*,
949 116(8), doi:10.1029/2010JD015330, 2011.
- 950 Brown, R. D. and Robinson, D. A.: Northern Hemisphere spring snow cover variability and
951 change over 1922-2010 including an assessment of uncertainty, *Cryosphere*, 5(1), 219–229,
952 doi:10.5194/tc-5-219-2011, 2011.
- 953 Campanelli, M., Estellés, V., Tomasi, C., Nakajima, T., Malvestuto, V. and Martínez-Lozano, J.
954 A.: Application of the SKYRAD Improved Langley plot method for the in situ calibration of
955 CIMEL Sun-sky photometers., *Appl. Opt.*, 46(14), 2688–702, doi:10.1364/AO.46.002688, 2007.
- 956 Chapman, E. G., Gustafson, W. I., Easter, R. C., Barnard, J. C., Ghan, S. J., Pekour, M. S. and
957 Fast, J. D.: Coupling aerosol-cloud-radiative processes in the WRF-Chem model: Investigating
958 the radiative impact of elevated point sources, *Atmos. Chem. Phys.*, 9(3), 945–964,
959 doi:10.5194/acp-9-945-2009, 2009.
- 960 Conway, H., Gades, A. and Raymond, C. F.: Albedo of dirty snow during conditions of melt,
961 *Water Resour. Res.*, 32(6), 1713–1718, doi:10.1029/96WR00712, 1996.
- 962 Dang, C., Warren, S. G., Fu, Q., Doherty, S. J., Sturm, M. and Su, J.: Measurements of light-
963 absorbing particles in snow across the Arctic, North America, and China: Effects on surface
964 albedo, *J. Geophys. Res. Atmos.*, 122(19), 10149–10168, doi:10.1002/2017JD027070, 2017.
- 965 Dentener, F., Kinne, S., Bond, T., Boucher, O., Cofala, J., Generoso, S., Ginoux, P., Gong, S.,
966 Hoelzemann, J. J., Ito, A., Marelli, L., Penner, J. E., Putaud, J. P., Textor, C., Schulz, M., Van
967 Der Werf, G. R. and Wilson, J.: Emissions of primary aerosol and precursor gases in the years
968 2000 and 1750 prescribed data-sets for AeroCom, *Atmos. Chem. Phys.*, 6(12), 4321–4344,
969 doi:10.5194/acp-6-4321-2006, 2006.
- 970 Doherty, S. J., Warren, S. G., Grenfell, T. C., Clarke, A. D. and Brandt, R. E.: Light-absorbing
971 impurities in Arctic snow, *Atmos. Chem. Phys.*, 10(23), 11647–11680, doi:10.5194/acp-10-
972 11647-2010, 2010.
- 973 Doherty, S. J., Grenfell, T. C., Forsström, S., Hegg, D. L., Brandt, R. E. and Warren, S. G.:
974 Observed vertical redistribution of black carbon and other insoluble light-absorbing particles in
975 melting snow, *J. Geophys. Res. Atmos.*, 118(11), 5553–5569, doi:10.1002/jgrd.50235, 2013.
- 976 Dozier, J., Painter, T. H., Rittger, K. and Frew, J. E.: Time-space continuity of daily maps of
977 fractional snow cover and albedo from MODIS, *Adv. Water Resour.*, 31(11), 1515–1526,
978 doi:10.1016/j.advwatres.2008.08.011, 2008.
- 979 Dubovik, O., Smirnov, A., Holben, B. N., King, M. D., Kaufman, Y. J., Eck, T. F. and Slutsker,
980 I.: Accuracy assessments of aerosol optical properties retrieved from Aerosol Robotic Network
981 (AERONET) Sun and sky radiance measurements, *J. Geophys. Res. Atmos.*, 105(D8), 9791–
982 9806, doi:10.1029/2000JD900040, 2000.
- 983 Dumka, U. C., Kaskaoutis, D. G., Srivastava, M. K. and Devara, P. C. S.: Scattering and
984 absorption properties of near-surface aerosol over Gangetic-Himalayan region: The role of
985 boundary-layer dynamics and long-range transport, *Atmos. Chem. Phys.*, 15(3), 1555–1572,
986 doi:10.5194/acp-15-1555-2015, 2015.



- 987 Dyurgerov, M. B.: Mountain glaciers at the end of the twentieth century: Global analysis in
988 relation to climate and water cycle, *Polar Geogr.*, 25(4), 241–336,
989 doi:10.1080/10889370109377717, 2001.
- 990 Easter, R. C., Ghan, S. J., Zhang, Y., Saylor, R. D., Chapman, E. G., Laulainen, N. S., Abdul-
991 Razzak, H., Leung, L. R., Bian, X. and Zaveri, R. A.: MIRAGE: Model description and
992 evaluation of aerosols and trace gases, *J. Geophys. Res. D Atmos.*, 109(20),
993 doi:10.1029/2004JD004571, 2004.
- 994 Fan, J., Wang, Y., Rosenfeld, D. and Liu, X.: Review of Aerosol–Cloud Interactions:
995 Mechanisms, Significance, and Challenges, *J. Atmos. Sci.*, 73(11), 4221–4252,
996 doi:10.1175/JAS-D-16-0037.1, 2016.
- 997 Fast, J. D., Gustafson, W. I., Easter, R. C., Zaveri, R. A., Barnard, J. C., Chapman, E. G., Grell,
998 G. A. and Peckham, S. E.: Evolution of ozone, particulates, and aerosol direct radiative forcing
999 in the vicinity of Houston using a fully coupled meteorology-chemistry-aerosol model, *J.*
1000 *Geophys. Res. Atmos.*, 111(21), doi:10.1029/2005JD006721, 2006.
- 1001 Flanner, M. G. and Zender, C. S.: Snowpack radiative heating: Influence on Tibetan Plateau
1002 climate, *Geophys. Res. Lett.*, 32(6), 1–5, doi:10.1029/2004GL022076, 2005.
- 1003 Flanner, M. G., Zender, C. S., Randerson, J. T. and Rasch, P. J.: Present-day climate forcing and
1004 response from black carbon in snow, *J. Geophys. Res. Atmos.*, 112(11),
1005 doi:10.1029/2006JD008003, 2007.
- 1006 Flanner, M. G., Zender, C. S., Hess, P. G., Mahowald, N. M., Painter, T. H., Ramanathan, V. and
1007 Rasch, P. J.: Springtime warming and reduced snow cover from carbonaceous particles, *Atmos.*
1008 *Chem. Phys.*, 9(7), 2481–2497, doi:10.5194/acp-9-2481-2009, 2009.
- 1009 Flanner, M. G., Liu, X., Zhou, C., Penner, J. E. and Jiao, C.: Enhanced solar energy absorption
1010 by internally-mixed black carbon in snow grains, *Atmos. Chem. Phys.*, 12(10), 4699–4721,
1011 doi:10.5194/acp-12-4699-2012, 2012.
- 1012 Gautam, R., Hsu, N. C., Lau, W. K. M. and Yasunari, T. J.: Satellite observations of desert dust-
1013 induced Himalayan snow darkening, *Geophys. Res. Lett.*, 40(5), 988–993,
1014 doi:10.1002/grl.50226, 2013.
- 1015 Gertler, C. G., Puppala, S. P., Panday, A., Stumm, D. and Shea, J.: Black carbon and the
1016 Himalayan cryosphere: A review, *Atmos. Environ.*, 125, 404–417,
1017 doi:10.1016/j.atmosenv.2015.08.078, 2016.
- 1018 Ghatak, D., Sinsky, E. and Miller, J.: Role of snow-albedo feedback in higher elevation warming
1019 over the Himalayas, Tibetan Plateau and Central Asia, *Environ. Res. Lett.*, 9(11),
1020 doi:10.1088/1748-9326/9/11/114008, 2014.
- 1021 Ginot, P., Dumont, M., Lim, S., Patris, N., Taupin, J. D., Wagnon, P., Gilbert, A., Arnaud, Y.,
1022 Marinoni, A., Bonasoni, P. and Laj, P.: A 10 year record of black carbon and dust from a Mera
1023 Peak ice core (Nepal): Variability and potential impact on melting of Himalayan glaciers,
1024 *Cryosphere*, 8(4), 1479–1496, doi:10.5194/tc-8-1479-2014, 2014.
- 1025 Ginoux, P., Chin, M., Tegen, I., Prospero, J. M., Holben, B., Dubovik, O. and Lin, S.-J.: Sources
1026 and distributions of dust aerosols simulated with the GOCART model, *J. Geophys. Res. Atmos.*,



- 1027 106(D17), 20255–20273, doi:10.1029/2000JD000053, 2001.
- 1028 Gustafson, W. I., Chapman, E. G., Ghan, S. J., Easter, R. C. and Fast, J. D.: Impact on modeled
1029 cloud characteristics due to simplified treatment of uniform cloud condensation nuclei during
1030 NEAQS 2004, *Geophys. Res. Lett.*, 34(19), doi:10.1029/2007GL030021, 2007.
- 1031 Hadley, O. L. and Kirchstetter, T. W.: Black-carbon reduction of snow albedo, *Nat. Clim.*
1032 *Chang.*, 2(6), 437–440, doi:10.1038/nclimate1433, 2012.
- 1033 Hansen, J. and Nazarenko, L.: Soot climate forcing via snow and ice albedos, *Proc. Natl. Acad.*
1034 *Sci.*, 101(2), 423–428, doi:10.1073/pnas.2237157100, 2004.
- 1035 Hansen, J., Sato, M. and Ruedy, R.: Radiative forcing and climate response, *J. Geophys. Res.*
1036 *Atmos.*, 102(D6), 6831–6864, doi:10.1029/96JD03436, 1997.
- 1037 He, C., Flanner, M. G., Chen, F., Barlage, M., Liou, K. N., Kang, S., Ming, J. and Qian, Y.:
1038 Black carbon-induced snow albedo reduction over the Tibetan Plateau: Uncertainties from snow
1039 grain shape and aerosol-snow mixing state based on an updated SNICAR model, *Atmos. Chem.*
1040 *Phys.*, 18(15), 11507–11527, doi:10.5194/acp-18-11507-2018, 2018.
- 1041 Hess, M., Koepke, P. and Schult, I.: Optical Properties of Aerosols and Clouds: The Software
1042 Package OPAC, *Bull. Am. Meteorol. Soc.*, 79(5), 831–844, doi:10.1175/1520-
1043 0477(1998)079<0831:OPOAAC>2.0.CO;2, 1998.
- 1044 Holben, B. N., Eck, T. F., Slutsker, I., Tanré, D., Buis, J. P., Setzer, A., Vermote, E., Reagan, J.
1045 A., Kaufman, Y. J., Nakajima, T., Lavenu, F., Jankowiak, I. and Smirnov, A.: AERONET—A
1046 Federated Instrument Network and Data Archive for Aerosol Characterization, *Remote Sens.*
1047 *Environ.*, 66(1), 1–16, doi:10.1016/S0034-4257(98)00031-5, 1998.
- 1048 Hu, Z., Zhao, C., Huang, J., Leung, L. R., Qian, Y., Yu, H., Huang, L. and Kalashnikova, O. V.:
1049 Trans-Pacific transport and evolution of aerosols: Evaluation of quasi-global WRF-Chem
1050 simulation with multiple observations, *Geosci. Model Dev.*, 9(5), 1725–1746, doi:10.5194/gmd-
1051 9-1725-2016, 2016.
- 1052 Immerzeel, W. W., Van Beek, L. P. H. and Bierkens, M. F. P.: Climate change will affect the
1053 asian water towers, *Science* (80-.), 328(5984), 1382–1385, doi:10.1126/science.1183188, 2010.
- 1054 IPCC: Climate change 2013: The physical science basis, *Contrib. Work. Gr. I to Fifth Assess.*
1055 *Rep. Intergov. Panel Clim. Chang.*, 33, doi:10.1017/CBO9781107415324, 2013.
- 1056 Jacobi, H. W., Lim, S., Ménégos, M., Ginot, P., Laj, P., Bonasoni, P., Stocchi, P., Marinoni, A.
1057 and Arnaud, Y.: Black carbon in snow in the upper Himalayan Khumbu Valley, Nepal:
1058 Observations and modeling of the impact on snow albedo, melting, and radiative forcing,
1059 *Cryosphere*, 9(4), 1685–1699, doi:10.5194/tc-9-1685-2015, 2015.
- 1060 Jayarathne, T., Stockwell, C. E., Bhave, P. V., Praveen, P. S., Rathnayake, C. M., Md Islam, R.,
1061 Panday, A. K., Adhikari, S., Maharjan, R., Douglas Goetz, J., Decarlo, P. F., Saikawa, E.,
1062 Yokelson, R. J. and Stone, E. A.: Nepal Ambient Monitoring and Source Testing Experiment
1063 (NAMaSTE): Emissions of particulate matter from wood-and dung-fueled cooking fires, garbage
1064 and crop residue burning, brick kilns, and other sources, *Atmos. Chem. Phys.*, 18(3), 2259–2286,
1065 doi:10.5194/acp-18-2259-2018, 2018.



- 1066 Ji, Z. M.: Modeling black carbon and its potential radiative effects over the Tibetan Plateau, *Adv.*
1067 *Clim. Chang. Res.*, 7(3), 139–144, doi:10.1016/j.accre.2016.10.002, 2016.
- 1068 Kaser, G., Grosshauser, M. and Marzeion, B.: Contribution potential of glaciers to water
1069 availability in different climate regimes, *Proc. Natl. Acad. Sci.*, 107(47), 20223–20227,
1070 doi:10.1073/pnas.1008162107, 2010.
- 1071 Kaspari, S., Painter, T. H., Gysel, M., Skiles, S. M. and Schwikowski, M.: Seasonal and
1072 elevational variations of black carbon and dust in snow and ice in the Solu-Khumbu, Nepal and
1073 estimated radiative forcings, *Atmos. Chem. Phys.*, 14(15), 8089–8103, doi:10.5194/acp-14-8089-
1074 2014, 2014.
- 1075 Khan, A. A., Pant, N. C., Sarkar, A., Tandon, S. K., Thamban, M. and Mahalinganathan, K.: The
1076 Himalayan cryosphere: A critical assessment and evaluation of glacial melt fraction in the
1077 Bhagirathi basin, *Geosci. Front.*, 8(1), 107–115, doi:10.1016/j.gsf.2015.12.009, 2017.
- 1078 Kopacz, M., Mauzerall, D. L., Wang, J., Leibensperger, E. M., Henze, D. K. and Singh, K.:
1079 Origin and radiative forcing of black carbon transported to the Himalayas and Tibetan Plateau,
1080 *Atmos. Chem. Phys.*, 11(6), 2837–2852, doi:10.5194/acp-11-2837-2011, 2011.
- 1081 Kulkarni, A. V., Rathore, B. P. and Singh, S. K.: Distribution of seasonal snow cover in central
1082 and western Himalaya, *Ann. Glaciol.*, 51(54), 123–128, doi:10.3189/172756410791386445,
1083 2010.
- 1084 Lau, K. M., Kim, M. K. and Kim, K. M.: Asian summer monsoon anomalies induced by aerosol
1085 direct forcing: The role of the Tibetan Plateau, *Clim. Dyn.*, 26(7–8), 855–864,
1086 doi:10.1007/s00382-006-0114-z, 2006.
- 1087 Lau, W. K. M., Kim, M. K., Kim, K. M. and Lee, W. S.: Enhanced surface warming and
1088 accelerated snow melt in the Himalayas and Tibetan Plateau induced by absorbing aerosols,
1089 *Environ. Res. Lett.*, 5(2), doi:10.1088/1748-9326/5/2/025204, 2010.
- 1090 Levy, R. C., Remer, L. A., Mattoo, S., Vermote, E. F. and Kaufman, Y. J.: Second-generation
1091 operational algorithm: Retrieval of aerosol properties over land from inversion of Moderate
1092 Resolution Imaging Spectroradiometer spectral reflectance, *J. Geophys. Res. Atmos.*, 112(13),
1093 doi:10.1029/2006JD007811, 2007.
- 1094 Levy, R. C., Remer, L. A., Kleidman, R. G., Mattoo, S., Ichoku, C., Kahn, R. and Eck, T. F.:
1095 Global evaluation of the Collection 5 MODIS dark-target aerosol products over land, *Atmos.*
1096 *Chem. Phys.*, 10(21), 10399–10420, doi:10.5194/acp-10-10399-2010, 2010.
- 1097 Li, Z., Lau, W. K. M., Ramanathan, V., Wu, G., Ding, Y., Manoj, M. G., Liu, J., Qian, Y., Li, J.,
1098 Zhou, T., Fan, J., Rosenfeld, D., Ming, Y., Wang, Y., Huang, J., Wang, B., Xu, X., Lee, S. S.,
1099 Cribb, M., Zhang, F., Yang, X., Zhao, C., Takemura, T., Wang, K., Xia, X., Yin, Y., Zhang, H.,
1100 Guo, J., Zhai, P. M., Sugimoto, N., Babu, S. S. and Brasseur, G. P.: Aerosol and monsoon
1101 climate interactions over Asia, *Rev. Geophys.*, 54(4), 866–929, doi:10.1002/2015RG000500,
1102 2016.
- 1103 Marcq, S., Laj, P., Roger, J. C., Villani, P., Sellegri, K., Bonasoni, P., Marinoni, A., Cristofanelli,
1104 P., Verza, G. P. and Bergin, M.: Aerosol optical properties and radiative forcing in the high
1105 Himalaya based on measurements at the Nepal Climate Observatory-Pyramid site (5079 m a.s.l.),



- 1106 Atmos. Chem. Phys., 10(13), 5859–5872, doi:10.5194/acp-10-5859-2010, 2010.
- 1107 Ménégot, M., Krinner, G., Balkanski, Y., Boucher, O., Cozic, A., Lim, S., Ginot, P., Laj, P.,
1108 Gallée, H., Wagnon, P., Marinoni, A. and Jacobi, H. W.: Snow cover sensitivity to black carbon
1109 deposition in the Himalayas: From atmospheric and ice core measurements to regional climate
1110 simulations, Atmos. Chem. Phys., 14(8), 4237–4249, doi:10.5194/acp-14-4237-2014, 2014.
- 1111 Menon, S., Koch, D., Beig, G., Sahu, S., Fasullo, J. and Orlikowski, D.: Black carbon aerosols
1112 and the third polar ice cap, Atmos. Chem. Phys., 10(10), 4559–4571, doi:10.5194/acp-10-4559-
1113 2010, 2010.
- 1114 Ming, J., Cachier, H., Xiao, C., Qin, D., Kang, S., Hou, S. and Xu, J.: Black carbon record based
1115 on a shallow Himalayan ice core and its climatic implications, Atmos. Chem. Phys., 8(5), 1343–
1116 1352, doi:10.5194/acp-8-1343-2008, 2008.
- 1117 Mlawer, E. J., Taubman, S. J., Brown, P. D., Iacono, M. J. and Clough, S. A.: Radiative transfer
1118 for inhomogeneous atmospheres: RRTM, a validated correlated-k model for the longwave, J.
1119 Geophys. Res. Atmos., 102(D14), 16663–16682, doi:10.1029/97JD00237, 1997.
- 1120 Nair, V. S., Babu, S. S., Moorthy, K. K., Sharma, A. K., Marinoni, A. and Ajai: Black carbon
1121 aerosols over the Himalayas: Direct and surface albedo forcing, Tellus, Ser. B Chem. Phys.
1122 Meteorol., 65(1), doi:10.3402/tellusb.v65i0.19738, 2013.
- 1123 Nakajima, T., Tonna, G., Rao, R., Boi, P., Kaufman, Y. and Holben, B.: Use of sky brightness
1124 measurements from ground for remote sensing of particulate polydispersions, Appl. Opt., 35(15),
1125 2672, doi:10.1364/AO.35.002672, 1996.
- 1126 Ningombam, S. S., Srivastava, A. K., Bagare, S. P., Singh, R. B., Kanawade, V. P. and Dorjey,
1127 N.: Assessment of aerosol optical and micro-physical features retrieved from direct and diffuse
1128 solar irradiance measurements from Skyradiometer at a high altitude station at Merak:
1129 Assessment of aerosol optical features from Merak, Environ. Sci. Pollut. Res., 22(21), 16610–
1130 16619, doi:10.1007/s11356-015-4788-9, 2015.
- 1131 Niu, H., Kang, S., Wang, H., Zhang, R., Lu, X., Qian, Y., Paudyal, R., Wang, S., Shi, X. and
1132 Yan, X.: Seasonal variation and light absorption property of carbonaceous aerosol in a typical
1133 glacier region of the southeastern Tibetan Plateau, Atmos. Chem. Phys., 18(9), 6441–6460,
1134 doi:10.5194/acp-18-6441-2018, 2018.
- 1135 Oleson, K. W., Lawrence, D. M., Gordon, B., Flanner, M. G., Kluzek, E., Peter, J., Levis, S.,
1136 Swenson, S. C., Thornton, E. and Feddema, J.: Technical description of version 4.0 of the
1137 Community Land Model (CLM)., 2010.
- 1138 Painter, T. H., Rittger, K., McKenzie, C., Slaughter, P., Davis, R. E. and Dozier, J.: Retrieval of
1139 subpixel snow covered area, grain size, and albedo from MODIS, Remote Sens. Environ.,
1140 113(4), 868–879, doi:10.1016/j.rse.2009.01.001, 2009.
- 1141 Painter, T. H., Bryant, A. C. and McKenzie Skiles, S.: Radiative forcing by light absorbing
1142 impurities in snow from MODIS surface reflectance data, Geophys. Res. Lett., 39(17),
1143 doi:10.1029/2012GL052457, 2012.
- 1144 Painter, T. H., Seidel, F. C., Bryant, A. C., McKenzie Skiles, S. and Rittger, K.: Imaging
1145 spectroscopy of albedo and radiative forcing by light-absorbing impurities in mountain snow, J.



- 1146 Geophys. Res. Atmos., 118(17), 9511–9523, doi:10.1002/jgrd.50520, 2013.
- 1147 Pfeffer, W. T., Arendt, A. A., Bliss, A., Bolch, T., Cogley, J. G., Gardner, A. S., Hagen, J. O.,
1148 Hock, R., Kaser, G., Kienholz, C., Miles, E. S., Moholdt, G., Mölg, N., Paul, F., Radić, V.,
1149 Rastner, P., Raup, B. H., Rich, J., Sharp, M. J., Andreassen, L. M., Bajracharya, S., Barrand, N.
1150 E., Beedle, M. J., Berthier, E., Bhambri, R., Brown, I., Burgess, D. O., Burgess, E. W.,
1151 Cawkwell, F., Chinn, T., Copland, L., Cullen, N. J., Davies, B., De Angelis, H., Fountain, A. G.,
1152 Frey, H., Giffen, B. A., Glasser, N. F., Gurney, S. D., Hagg, W., Hall, D. K., Haritashya, U. K.,
1153 Hartmann, G., Herreid, S., Howat, I., Jiskoot, H., Khromova, T. E., Klein, A., Kohler, J., König,
1154 M., Kriegel, D., Kutuzov, S., Lavrentiev, I., Le Bris, R., Li, X., Manley, W. F., Mayer, C.,
1155 Menounos, B., Mercer, A., Mool, P., Negrete, A., Nosenko, G., Nuth, C., Osmonov, A.,
1156 Pettersson, R., Racoviteanu, A., Ranzi, R., Sarikaya, M. A., Schneider, C., Sigurdsson, O.,
1157 Sirguey, P., Stokes, C. R., Wheate, R., Wolken, G. J., Wu, L. Z. and Wyatt, F. R.: The randolph
1158 glacier inventory: A globally complete inventory of glaciers, *J. Glaciol.*, 60(221), 537–552,
1159 doi:10.3189/2014JoG13J176, 2014.
- 1160 Prasad, A. K., S. Yang, K. H., El-Askary, H. M. and Kafatos, M.: Melting of major Glaciers in
1161 the western Himalayas: Evidence of climatic changes from long term MSU derived tropospheric
1162 temperature trend (1979–2008), *Ann. Geophys.*, 27(12), 4505–4519, doi:10.5194/angeo-27-4505-
1163 2009, 2009.
- 1164 Qian, Y., Gong, D., Fan, J., Ruby Leung, L., Bennartz, R., Chen, D. and Wang, W.: Heavy
1165 pollution suppresses light rain in China: Observations and modeling, *J. Geophys. Res. Atmos.*,
1166 114(15), doi:10.1029/2008JD011575, 2009.
- 1167 Qian, Y., Flanner, M. G., Leung, L. R. and Wang, W.: Sensitivity studies on the impacts of
1168 Tibetan Plateau snowpack pollution on the Asian hydrological cycle and monsoon climate,
1169 *Atmos. Chem. Phys.*, 11(5), 1929–1948, doi:10.5194/acp-11-1929-2011, 2011.
- 1170 Qian, Y., Wang, H., Zhang, R., Flanner, M. G. and Rasch, P. J.: A sensitivity study on modeling
1171 black carbon in snow and its radiative forcing over the Arctic and Northern China, *Environ. Res.*
1172 *Let.*, 9(6), doi:10.1088/1748-9326/9/6/064001, 2014.
- 1173 Qian, Y., Yasunari, T. J., Doherty, S. J., Flanner, M. G., Lau, W. K. M., Ming, J., Wang, H.,
1174 Wang, M., Warren, S. G. and Zhang, R.: Light-absorbing particles in snow and ice:
1175 Measurement and modeling of climatic and hydrological impact, *Adv. Atmos. Sci.*, 32(1), 64–
1176 91, doi:10.1007/s00376-014-0010-0, 2015.
- 1177 Raatikainen, T., Hyvärinen, A. P., Hatakka, J., Panwar, T. S., Hooda, R. K., Sharma, V. P. and
1178 Lihavainen, H.: The effect of boundary layer dynamics on aerosol properties at the Indo-
1179 Gangetic plains and at the foothills of the Himalayas, *Atmos. Environ.*, 89, 548–555,
1180 doi:10.1016/j.atmosenv.2014.02.058, 2014.
- 1181 V. Ramanathan and G. Carmichael: Global and regional climate changes due to black carbon,
1182 *Nat. Geosci.*, 1(January), 221–227, doi:10.1038/ngeo156, 2008.
- 1183 Ramanathan, V., Crutzen, P. J., Kiehl, J. T., Rosenfeld, D., Haywood, J., Boucher, O., Kaufman,
1184 Y. J., Collins, W. D., Hansen, J. E., Sato, M., Ruedy, R., Kiehl, J. T., Trenberth, K. E., Crutzen,
1185 P. J., Andreae, M. O., Charlson, R. J., Langner, J., Rodhe, H., Leovy, C. B., Warren, S. G.,
1186 Clarke, A. D., Charlson, R. J., Grassl, H., Ogren, J. A., Charlson, R. J., Jayaraman, A., Satheesh,



- 1187 S. K., Ramanathan, V., Jacobson, M. J., Russell, P. B., Eck, T. F., Holben, B. N., Slutsker, I.,
1188 Setzer, A., Raes, F., Bates, T., McGovern, F., Liedekerke, M. Van, Rajeev, K., Ramanathan, V.,
1189 Meywerk, J., Lelieveld, J., Ramanathan, V., Konzelmann, T., Cahoon, D. R., Whitlock, C. H.,
1190 Twomey, S., Novakov, T., Penner, J. E., Charlson, R. J., Martin, G. M., Johnson, W., Spice, A.,
1191 Guiltepe, I., Issac, G. A., Leaitch, W. R., Banic, C. M., Pawlowska, H., Brenguier, J.-L., Taylor,
1192 J. P., McHaffie, A., Coakley, J. A., Bernstein, R. L., Durkey, P. A., Kaufman, Y. J., Fraser, R.
1193 S., Nakajima, T., Higurashi, A., Kawamoto, K., Penner, J. E., Hansen, J., Sato, M., Ruedy, R.,
1194 Laci, A., Oinas, V., Warner, J. J., Rosenfeld, D., _____, Rudich, Y., Lahav, R., Levitus, S.,
1195 Stanhill, G., Cohen, S., Gilgen, H., Wild, M., Ohmura, A., Ramaswamy, V., Chen, C. T., Meehl,
1196 G. A., Washington, W. M., Erickson, D. J., Briegleb, B. P., Jaumann, P. J., Michell, J. F. B.,
1197 Johns, T. C., Roeckner, E., Bengtsson, L., Feichter, J., et al.: Aerosols, climate, and the
1198 hydrological cycle., *Science*, 294(5549), 2119–24, doi:10.1126/science.1064034, 2001.
- 1199 Ramanathan, V., Ramana, M. V., Roberts, G., Kim, D., Corrigan, C., Chung, C. and Winker, D.:
1200 Warming trends in Asia amplified by brown cloud solar absorption, *Nature*, 448(7153), 575–578,
1201 doi:10.1038/nature06019, 2007.
- 1202 Ren, D. and Karoly, D.: Comparison of glacier-inferred temperatures with observations and
1203 climate model simulations, *Geophys. Res. Lett.*, 33(23), doi:10.1029/2006GL027856, 2006.
- 1204 Ren, J., Jing, Z., Pu, J. and Qin, X.: Glacier variations and climate change in the central
1205 Himalaya over the past few decades, in *Annals of Glaciology*, vol. 43, pp. 218–222., 2006.
- 1206 Rittger, K., Painter, T. H. and Dozier, J.: Assessment of methods for mapping snow cover from
1207 MODIS, *Adv. Water Resour.*, 51, 367–380, doi:10.1016/j.advwatres.2012.03.002, 2013.
- 1208 Rittger, K., Bair, E. H., Kahl, A. and Dozier, J.: Spatial estimates of snow water equivalent from
1209 reconstruction, *Adv. Water Resour.*, 94, 345–363, doi:10.1016/j.advwatres.2016.05.015, 2016.
- 1210 Sarangi, C., Tripathi, S. N., Kanawade, V. P., Koren, I. and Sivanand Pai, D.: Investigation of
1211 the aerosol-cloud-rainfall association over the Indian summer monsoon region, *Atmos. Chem.*
1212 *Phys.*, 17(8), doi:10.5194/acp-17-5185-2017, 2017.
- 1213 Schmale, J., Flanner, M., Kang, S., Sprenger, M., Zhang, Q., Guo, J., Li, Y., Schwikowski, M.
1214 and Farinotti, D.: Modulation of snow reflectance and snowmelt from Central Asian glaciers by
1215 anthropogenic black carbon, *Sci. Rep.*, 7, doi:10.1038/srep40501, 2017.
- 1216 Shrestha, A. B., Wake, C. P., Mayewski, P. A. and Dibb, J. E.: Maximum temperature trends in
1217 the Himalaya and its vicinity: An analysis based on temperature records from Nepal for the
1218 period 1971-94, *J. Clim.*, 12(9), 2775–2786, doi:10.1175/1520-
1219 0442(1999)012<2775:MTTITH>2.0.CO;2, 1999.
- 1220 Simard, M., Pinto, N., Fisher, J. B. and Baccini, A.: Mapping forest canopy height globally with
1221 spaceborne lidar, *J. Geophys. Res. Biogeosciences*, 116(4), doi:10.1029/2011JG001708, 2011.
- 1222 Singh, P. and Bengtsson, L.: Hydrological sensitivity of a large Himalayan basin to climate
1223 change, *Hydrol. Process.*, 18(13), 2363–2385, doi:10.1002/hyp.1468, 2004.
- 1224 Skiles, S. M., Painter, T. H., Deems, J. S., Bryant, A. C. and Landry, C. C.: Dust radiative
1225 forcing in snow of the Upper Colorado River Basin: 2. Interannual variability in radiative forcing
1226 and snowmelt rates, *Water Resour. Res.*, 48(7), doi:10.1029/2012WR011986, 2012.



- 1227 Skiles, S. M., Painter, T. H., Belnap, J., Holland, L., Reynolds, R. L., Goldstein, H. L. and Lin,
1228 J.: Regional variability in dust-on-snow processes and impacts in the Upper Colorado River
1229 Basin, *Hydrol. Process.*, 29(26), 5397–5413, doi:10.1002/hyp.10569, 2015.
- 1230 Skiles, S. M. K. and Painter, T.: Daily evolution in dust and black carbon content, snow grain
1231 size, and snow albedo during snowmelt, Rocky Mountains, Colorado, *J. Glaciol.*, 63(237), 118–
1232 132, doi:10.1017/jog.2016.125, 2017.
- 1233 Svensson, J., Ström, J., Kivekäs, N., Dkhar, N. B., Tayal, S., Sharma, V. P., Jutila, A., Backman,
1234 J., Virkkula, A., Ruppel, M., Hyvärinen, A., Kontu, A., Backman, J., Leppäranta, M., Hooda, R.
1235 K., Korhola, A., Asmi, E. and Lihavainen, H.: Light-Absorption of dust and elemental carbon in
1236 snow in the Indian Himalayas and the Finnish Arctic, *Atmos. Meas. Tech.*, 11(3), 1403–1416,
1237 doi:10.5194/amt-11-1403-2018, 2018.
- 1238 Toon, O. B., McKay, C. P., Ackerman, T. P. and Santhanam, K.: Rapid calculation of radiative
1239 heating rates and photodissociation rates in inhomogeneous multiple scattering atmospheres, *J.*
1240 *Geophys. Res.*, 94(D13), 16287, doi:10.1029/JD094iD13p16287, 1989.
- 1241 Tripathi, S. N., Dey, S., Chandel, A., Srivastava, S., Singh, R. P. and Holben, B. N.: Comparison
1242 of MODIS and AERONET derived aerosol optical depth over the Ganga Basin, India, *Ann.*
1243 *Geophys.*, 23(4), 1093–1101, doi:10.5194/angeo-23-1093-2005, 2005.
- 1244 Wake, C. P., Mayewski, P. A., Li, Z., Han, J. and Qin, D.: Modern eolian dust deposition in
1245 central Asia, *Tellus B Chem. Phys. Meteorol.*, 46(3), 220–233, doi:10.3402/tellusb.v46i3.15793,
1246 1994.
- 1247 Wang, B., Bao, Q., Hoskins, B., Wu, G. and Liu, Y.: Tibetan Plateau warming and precipitation
1248 changes in East Asia, *Geophys. Res. Lett.*, 35(14), doi:10.1029/2008GL034330, 2008.
- 1249 Wang, M., Xu, B., Cao, J., Tie, X., Wang, H., Zhang, R., Qian, Y., Rasch, P. J., Zhao, S., Wu,
1250 G., Zhao, H., Joswiak, D. R., Li, J. and Xie, Y.: Carbonaceous aerosols recorded in a
1251 southeastern Tibetan glacier: Analysis of temporal variations and model estimates of sources and
1252 radiative forcing, *Atmos. Chem. Phys.*, 15(3), 1191–1204, doi:10.5194/acp-15-1191-2015,
1253 2015a.
- 1254 Wang, M., Xu, B., Kaspari, S. D., Gleixner, G., Schwab, V. F., Zhao, H., Wang, H. and Yao, P.:
1255 Century-long record of black carbon in an ice core from the Eastern Pamirs: Estimated
1256 contributions from biomass burning, *Atmos. Environ.*, 115, 79–88,
1257 doi:10.1016/j.atmosenv.2015.05.034, 2015b.
- 1258 Warren, S. G.: Can black carbon in snow be detected by remote sensing?, *J. Geophys. Res.*
1259 *Atmos.*, 118(2), 779–786, doi:10.1029/2012JD018476, 2013.
- 1260 Warren, S. G. and Wiscombe, W. J.: A Model for the Spectral Albedo of Snow. II: Snow
1261 Containing Atmospheric Aerosols, *J. Atmos. Sci.*, 37(12), 2734–2745, doi:10.1175/1520-
1262 0469(1980)037<2734:AMFTSA>2.0.CO;2, 1980.
- 1263 Van Der Werf, G. R., Randerson, J. T., Giglio, L., Collatz, G. J., Mu, M., Kasibhatla, P. S.,
1264 Morton, D. C., Defries, R. S., Jin, Y. and Van Leeuwen, T. T.: Global fire emissions and the
1265 contribution of deforestation, savanna, forest, agricultural, and peat fires (1997-2009), *Atmos.*
1266 *Chem. Phys.*, 10(23), 11707–11735, doi:10.5194/acp-10-11707-2010, 2010.



- 1267 Xu, B., Cao, J., Hansen, J., Yao, T., Joswia, D. R., Wang, N., Wu, G., Wang, M., Zhao, H.,
1268 Yang, W., Liu, X. and He, J.: Black soot and the survival of Tibetan glaciers, *Proc. Natl. Acad.*
1269 *Sci.*, 106(52), 22114–22118, doi:10.1073/pnas.0910444106, 2009a.
- 1270 Xu, J., Grumbine, R. E., Shrestha, A., Eriksson, M., Yang, X., Wang, Y. and Wilkes, A.: The
1271 melting Himalayas: Cascading effects of climate change on water, biodiversity, and livelihoods,
1272 *Conserv. Biol.*, 23(3), 520–530, doi:10.1111/j.1523-1739.2009.01237.x, 2009b.
- 1273 Yao, T., Pu, J., Lu, A., Wang, Y. and Yu, W.: Recent Glacial Retreat and Its Impact on
1274 Hydrological Processes on the Tibetan Plateau, China, and Surrounding Regions, Arctic, Antarct.
1275 *Alp. Res.*, 39(4), 642–650, doi:10.1657/1523-0430(07-510)[YAO]2.0.CO;2, 2007.
- 1276 Yasunari, T. J., Bonasoni, P., Laj, P., Fujita, K., Vuillermoz, E., Marinoni, A., Cristofanelli, P.,
1277 Duchi, R., Tartari, G. and Lau, K. M.: Estimated impact of black carbon deposition during pre-
1278 monsoon season from Nepal Climate Observatory - Pyramid data and snow albedo changes over
1279 Himalayan glaciers, *Atmos. Chem. Phys.*, 10(14), 6603–6615, doi:10.5194/acp-10-6603-2010,
1280 2010a.
- 1281 Yasunari, T. J., Bonasoni, P., Laj, P., Fujita, K., Vuillermoz, E., Marinoni, A., Cristofanelli, P.,
1282 Duchi, R., Tartari, G. and Lau, K.-M.: Preliminary estimation of black carbon deposition from
1283 Nepal Climate Observatory-Pyramid data and its possible impact on snow albedo changes over
1284 Himalayan glaciers during the pre-monsoon season., *Atmos. Chem. Phys. Discuss.*, 10(4), 9291–
1285 9328 [online] Available from:
1286 [https://ezp.lib.unimelb.edu.au/login?url=https://search.ebscohost.com/login.aspx?direct=true&db](https://ezp.lib.unimelb.edu.au/login?url=https://search.ebscohost.com/login.aspx?direct=true&db=eih&AN=51503391&site=eds-live&scope=site)
1287 [=eih&AN=51503391&site=eds-live&scope=site](https://ezp.lib.unimelb.edu.au/login?url=https://search.ebscohost.com/login.aspx?direct=true&db=eih&AN=51503391&site=eds-live&scope=site), 2010b.
- 1288 Yasunari, T. J., Tan, Q., Lau, K. M., Bonasoni, P., Marinoni, A., Laj, P., Ménégoz, M.,
1289 Takemura, T. and Chin, M.: Estimated range of black carbon dry deposition and the related snow
1290 albedo reduction over Himalayan glaciers during dry pre-monsoon periods, *Atmos. Environ.*, 78,
1291 259–267, doi:10.1016/j.atmosenv.2012.03.031, 2013.
- 1292 Zaveri, R. A. and Peters, L. K.: A new lumped structure photochemical mechanism for large-
1293 scale applications, *J. Geophys. Res. Atmos.*, 104(D23), 30387–30415,
1294 doi:10.1029/1999JD900876, 1999.
- 1295 Zaveri, R. A., Easter, R. C., Fast, J. D. and Peters, L. K.: Model for Simulating Aerosol
1296 Interactions and Chemistry (MOSAIC), *J. Geophys. Res. Atmos.*, 113(13),
1297 doi:10.1029/2007JD008782, 2008.
- 1298 Zhang, Q., Streets, D. G., Carmichael, G. R., He, K. B., Huo, H., Kannari, A., Klimont, Z., Park,
1299 I. S., Reddy, S., Fu, J. S., Chen, D., Duan, L., Lei, Y., Wang, L. T. and Yao, Z. L.: Asian
1300 emissions in 2006 for the NASA INTEX-B mission, *Atmos. Chem. Phys.*, 9(14), 5131–5153,
1301 doi:10.5194/acp-9-5131-2009, 2009.
- 1302 Zhang, R., Wang, H., Qian, Y., Rasch, P. J., Easter, R. C., Ma, P. L., Singh, B., Huang, J. and
1303 Fu, Q.: Quantifying sources, transport, deposition, and radiative forcing of black carbon over the
1304 Himalayas and Tibetan Plateau, *Atmos. Chem. Phys.*, 15(11), 6205–6223, doi:10.5194/acp-15-
1305 6205-2015, 2015.
- 1306 Zhang, Y., Kang, S., Sprenger, M., Cong, Z., Gao, T., Li, C., Tao, S., Li, X., Zhong, X., Xu, M.,
1307 Meng, W., Neupane, B., Qin, X. and Sillanpää, M.: Black carbon and mineral dust in snow cover



- 1308 on the Tibetan Plateau, *Cryosph.*, 12(2), 413–431, doi:10.5194/tc-12-413-2018, 2018.
- 1309 Zhao, C., Liu, X., Leung, L. R. and Hagos, S.: Radiative impact of mineral dust on monsoon
1310 precipitation variability over West Africa, *Atmos. Chem. Phys.*, 11(5), 1879–1893,
1311 doi:10.5194/acp-11-1879-2011, 2011.
- 1312 Zhao, C., Leung, L. R., Easter, R., Hand, J. and Avise, J.: Characterization of speciated aerosol
1313 direct radiative forcing over California, *J. Geophys. Res. Atmos.*, 118(5), 2372–2388,
1314 doi:10.1029/2012JD018364, 2013a.
- 1315 Zhao, C., Chen, S., Leung, L. R., Qian, Y., Kok, J. F., Zaveri, R. A. and Huang, J.: Uncertainty
1316 in modeling dust mass balance and radiative forcing from size parameterization, *Atmos. Chem.*
1317 *Phys.*, 13(21), 10733–10753, doi:10.5194/acp-13-10733-2013, 2013b.
- 1318 Zhao, C., Hu, Z., Qian, Y., Ruby Leung, L., Huang, J., Huang, M., Jin, J., Flanner, M. G., Zhang,
1319 R., Wang, H., Yan, H., Lu, Z. and Streets, D. G.: Simulating black carbon and dust and their
1320 radiative forcing in seasonal snow: A case study over North China with field campaign
1321 measurements, *Atmos. Chem. Phys.*, 14(20), 11475–11491, doi:10.5194/acp-14-11475-2014,
1322 2014.
- 1323